

The three-dimensional Ising spin glass in an external magnetic field: the role of the silent majority

M Baity-Jesi^{1,2,3}, R A Baños^{3,4}, A Cruz^{3,4},
L A Fernandez^{1,3}, J M Gil-Narvion³, A Gordillo-Guerrero^{3,5},
D Iñiguez^{3,6}, A Maiorano^{2,3}, F Mantovani⁷, E Marinari⁸,
V Martin-Mayor^{1,3}, J Monforte-Garcia^{3,4},
A Muñoz Sudupe¹, D Navarro⁹, G Parisi⁸, S Perez-Gaviro³,
M Pivanti⁷, F Ricci-Tersenghi⁸, J J Ruiz-Lorenzo^{3,10},
S F Schifano¹¹, B Seoane^{2,3}, A Tarancon^{3,4}, R Tripiccione⁷
and D Yllanes^{2,3}

¹ Departamento de Física Teórica I, Universidad Complutense, E-28040 Madrid, Spain

² Dipartimento di Fisica, La Sapienza Università di Roma, I-00185 Roma, Italy

³ Instituto de Biocomputación y Física de Sistemas Complejos (BIFI), E-50009 Zaragoza, Spain

⁴ Departamento de Física Teórica, Universidad de Zaragoza, E-50009 Zaragoza, Spain

⁵ D. de Ingeniería Eléctrica, Electrónica y Automática, U. de Extremadura, E-10071, Cáceres, Spain

⁶ Fundación ARAID, Diputación General de Aragón, Zaragoza, Spain

⁷ Barcelona Supercomputing Center, E-08034 Barcelona, Spain

⁸ Dipartimento di Fisica, IPCF-CNR, UOS Roma Kerberos and INFN, La Sapienza Università di Roma, I-00185 Roma, Italy

⁹ D. de Ingeniería, Electrónica y Comunicaciones and I3A, U. de Zaragoza, E-50018 Zaragoza, Spain

¹⁰ Departamento de Física, Universidad de Extremadura, E-06071 Badajoz, Spain

¹¹ Dipartimento di Matematica e Informatica, Università di Ferrara and INFN, Ferrara, Italy

E-mail: marcobaityesi@fis.ucm.es, raquel.alvarez@unizar.es, andres@unizar.es, lsntnfp@ucm.es, jmgil@bifi.es, anto@unex.es, david.iniguez@bifi.es, andrea.maiorano@roma1.infn.it, filippo.mantovani@bsc.es, enzo.marinari@roma1.infn.it, vicmarti@ucm.es, jmonforte@bifi.es,

sudupe@fis.ucm.es, denis@unizar.es, giorgio.parisi@roma1.infn.it,
 spgaviro@unizar.es, pivanti@fe.infn.it, Federico.Ricci@roma1.infn.it,
 ruiz@unex.es, schifano@fe.infn.it, seoanebb@roma1.infn.it, tarancon@unizar.es,
 tripiccione@fe.infn.it and yllanesd@roma1.infn.it

Received 13 March 2014

Accepted for publication 27 March 2014

Published 16 May 2014

Online at stacks.iop.org/JSTAT/2014/P05014

doi:10.1088/1742-5468/2014/05/P05014

Abstract. We perform equilibrium parallel-tempering simulations of the 3D Ising Edwards–Anderson spin glass in a field, using the *Janus* computer. A traditional analysis shows no signs of a phase transition. However, we encounter dramatic fluctuations in the behaviour of the model: averages over all the data only describe the behaviour of a small fraction of the data. Therefore, we develop a new approach to study the equilibrium behaviour of the system, by classifying the measurements as a function of a conditioning variate. We propose a finite-size scaling analysis based on the probability distribution function of the conditioning variate, which may accelerate the convergence to the thermodynamic limit. In this way, we find a non-trivial spectrum of behaviours, where some of the measurements behave as the average, while the majority show signs of scale invariance. As a result, we can estimate the temperature interval where the phase transition in a field ought to lie, if it exists. Although this would-be critical regime is unreachable with present resources, the numerical challenge is finally well posed.

Keywords: disordered systems (theory), spin glasses (theory)

ArXiv ePrint: [1403.2622](https://arxiv.org/abs/1403.2622)

J. Stat. Mech. (2014) P05014

Contents

1. Introduction	3
2. Extended introduction: giant fluctuations and the silent minority	5
2.1. Foreword	5
2.2. No signs of a phase transition with common tools	5
2.3. Signs of a hidden behaviour	6
2.4. Giant fluctuations	7
3. Model and simulations	8
3.1. The model.	8
3.2. The simulations	9
4. Observables	9
5. Finite-size scaling	12

6. Conditional expectation values and variances	12
6.1. The conditioning variate.	12
6.2. Measurements against samples.	13
6.3. The selection of the conditioning variate.	14
6.3.1. A quantitative criterion.	14
6.3.2. Candidates for \hat{q}	15
7. Quantiles and a modified finite-size scaling ansatz	16
7.1. The $P(q_{\text{med}})$	17
8. Results	18
9. This is not an echo of the $h = 0$ transition	21
9.1. An escaping transition.	21
9.2. Scaling at $T = T_c(h = 0)$	23
10. Conclusions	24
Acknowledgments	25
Appendix A. Quantiles for different fields	25
A.1. Quantiles for $h = 0.1$	25
A.2. Quantiles for $h = 0$	27
Appendix B. Four-replica correlators	28
B.1. The effective anomalous dimension in the spin-glass phase	29
Appendix C. Technical details on the creation of quantiles	30
C.1. Creating the $P(\hat{q})$	30
C.2. Defining the quantiles	31
Appendix D. A caveat for the quantile description	32
Appendix E. Finding a privileged q	32
Appendix F. Quantiles with two-replica correlators	33
Appendix G. High-temperature extrapolation of the critical line	36
References	37

1. Introduction

Spin glasses are disordered magnetic alloys [1]. The most popular model for these alloys is the Edwards–Anderson model [2, 3], widely regarded as one of the simplest instances of a complex system [4]. The corresponding phase diagram is tridimensional: besides the temperature and the externally applied magnetic field, the space dimensionality also plays a crucial role [4].

Above the upper critical space dimension, $D_u = 6$, mean-field theory becomes quantitatively accurate [4]–[6]. As for most magnetic systems, time-reversal symmetry is spontaneously broken below a critical temperature T_c . However, the behaviour of mean-field spin glasses in an external field h is most peculiar¹². Although the external field explicitly breaks time-reversal symmetry at any temperature, de Almeida and Thouless have shown that a phase transition occurs also for $h > 0$ at the so-called dAT line, $T_c(h)$ [5]. The symmetry that is spontaneously broken at $T_c(h)$ is the abstract replica symmetry, which encodes a complex free-energy landscape [4], [7]–[9].

It is still unclear how much of the above picture (usually known as the replica symmetry breaking or RSB picture) is realized in our three-dimensional world. Some believe it should still apply without dramatic modifications [6, 10]. However, a dissenting school of thought, the so-called droplet picture, predicts no phase transition in a field as soon as one goes below six spatial dimensions [11]–[14]. Some recent developments of this debate are discussed in [10, 15, 16].

A rather obvious way out would be an experimental study of spin glasses in a field. Unfortunately, opposing indications have been observed regarding the existence of a phase transition [17]–[20].

The renormalization group approach to this problem also provides conflicting results. No fixed points were found by enforcing that the number of replicas of the replicated field theory be zero [21]. However, fixed points were found by relaxing this condition and using the most general Hamiltonian [22]. Reasoning along these lines, in [23] (see also [10]) the de Almeida–Thouless line was computed for D slightly below $D_u = 6$ (the upper critical dimension remains 6 when an external magnetic field is applied).

Equilibrium numerical simulations offer an alternative approach, which has already been effective in establishing that a phase transition does occur at zero field in the $D = 3$ Edwards–Anderson model [24, 25] (in agreement with experiments [26]). The same strategy has been followed for $h > 0$, with negative results [27, 28]. However, this cannot be the whole story: recent work in $D = 4$, hence below D_u , using a non-standard finite-size scaling method has found clear evidence for a dAT line [29]. Furthermore, one may try to interpolate between $D = 3$ and $D = 4$ by tuning long-range interactions in $D = 1$ chains [30, 31]. This approach suggests that a dAT might be present in $D = 4$, but not in $D = 3$ [32] (yet, see the criticism in [33]).

As the problem is still open, in [34] we undertook a dynamical study of the three-dimensional Edwards–Anderson spin glass with the *Janus* dedicated computer, an FPGA-based machine especially designed for Ising spin glass simulations [35]–[38]. We studied very large lattices ($L = 80$), in wide time scales (from an equivalent of ~ 1 ps to ~ 0.01 s), and gathered both equilibrium and non-equilibrium data. We focused on the increase of relaxation times and found a would-be dynamical transition, but at a suspiciously high temperature. A subsequent examination of the correlation length found a growth faster than predicted by the droplet theory, and slower than what RSB would expect. We also examined the problem from a supercooled liquid point of view [39]–[44], motivated by [45, 46]. At any rate, the study of the possible critical divergence of the correlation length allowed us to give upper bounds $T^{\text{up}}(h)$ to the possible transition

¹² The definition of h is given in section 3, equation (1).

line for the studied fields¹³. For further reference we recall that $T^{\text{up}}(h = 0.1) = 0.8$ and $T^{\text{up}}(h = 0.2) = T^{\text{up}}(h = 0.3) = 0.5$.

The impossibility of obtaining concluding evidence in [34] may be due to the fact that we did not reach low enough temperatures (our simulations fell out of equilibrium at temperatures T significantly higher than $T^{\text{up}}(h)$). In any case, a study of the equilibrium properties of the model is mandatory if one wants to understand the nature of the thermodynamic phases of the three-dimensional Edwards–Anderson spin glass in a field.

In this paper we report the result of equilibrium simulations performed on *Janus*, using lattices up to $L = 32$. Analogously to what has been already found in mean-field spin glasses on the de Almeida–Thouless line, we find extreme fluctuations in the model’s behaviour [47]. We will propose a method to tame these fluctuations, and we will find out that, although the average behaviour does not show any sign of a phase transition, this is not true for the medians of our observables, where we have indications of a possible phase transition at a temperature $T_c \lesssim T^{\text{up}}(h)$.

In section 2 we extend this introduction, giving an intuitive justification of why we deepened our analysis after finding no sign of a phase transition using the standard indicators. We define the model and explain how simulations were carried out in section 3. In section 4 we define the observables we measured, and we make brief comments on finite-size scaling in section 5. Sections 6 and 7 are dedicated to the description of the method we adopted to monitor extreme fluctuations. In section 8 we present our results, and in section 9 we show that they are not an echo of the zero-field transition. Finally, we give our conclusions in section 10. Further details are given in the appendices.

2. Extended introduction: giant fluctuations and the silent minority

2.1. Foreword

Since the bulk of this article will become technical in the description of a method that allows a classification of the data, we will first give a qualitative description of our results in terms of intuitive concepts. In this way, the reader will be more aware of the reasons that lead to the conception of the following analysis.

2.2. No signs of a phase transition with common tools

The most common way to locate a phase transition is to identify some observable R that benefits from scale invariance in the presence of a phase transition (for example the correlation length ξ_L measured in a lattice of size L , divided by L). This means that if we plot R as a function of the temperature, for many system sizes, all the curves will cross at the critical temperature T_c where the phase transition occurs. For sufficiently large systems, if the curves do not cross, there is no phase transition in the simulated temperature range (see sections 4 and 5 for details). The idea dates back to Nightingale [48] and Binder [49], and has been very successful in the study of disordered systems [25, 28], [50]–[54], [31], [55]–[57].

In our case, this type of analysis yields a clear result: there is no evidence of a crossing at the simulated temperatures, magnetic fields and sizes. This is clearly visible from figure 1, where the curves $\xi_L(T)/L$ and $R_{12}(T)$ (see (10) and (11) in section 4) should have

¹³ In [34] we studied a bimodal field, while in this paper h is constant. Notwithstanding, we will make comparisons with the bounds $T^{\text{up}}(h)$ by matching \bar{h}^2 in both models.

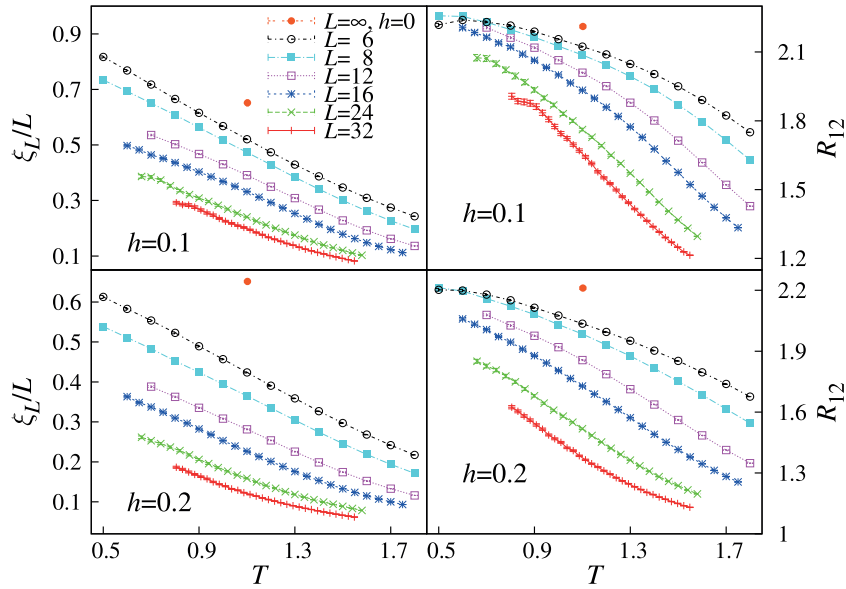


Figure 1. The figures on the left show the standard correlation length ξ_L in units of the lattice size L as a function of the temperature T , for all our lattice sizes. The magnetic fields are $h = 0.1$ (top) and $h = 0.2$ (bottom). If the lattices are large enough, in the presence of a second-order phase transition, the curves are expected to cross at a finite temperature $T_c(h)$. The figures on the right show the cumulant R_{12} , which in the presence of a magnetic field is a better indicator of a phase transition [29] for the same magnetic fields. At zero field the heights of the crossings (which are universal quantities) are indicated with a point at $T_c = 1.1019(29)$. They are $\xi_L/L(h = 0; T_c) = 0.6516(32)$ and $R_{12}(h = 0; T_c) = 2.211(6)$ [51]. In neither case do we observe signs of a crossing at the simulated temperatures, nor can we state that the curves will cross at lower temperature. The reader might remark that the curve for $L = 32$, $h = 0.1$ is not as smooth as one would expect from parallel-tempering simulations. The reason is twofold. On one hand the number of simulated samples is much smaller than for $L < 32$ and on the other hand temperature chaos, which is stronger for a larger lattice, is probably present [58].

some crossing point if we were in the presence of a phase transition. This is in complete qualitative agreement with earlier work on this model [27, 28].

2.3. Signs of a hidden behaviour

Although $\xi_L(T)/L$ is smaller for a larger lattice size, the coherence length ξ_L grows significantly even for our largest lattice sizes. For example, at $h = 0.2$, $T = 0.81$ we have $\xi_{16} = 6.09(4)$, $\xi_{24} = 7.63(9)$ and $\xi_{32} = 9.0(2)$. The noticeable size evolution implies that the asymptotic correlation length ξ_∞ is large compared with $L = 32$.

Also, we can examine the behaviour of the spin-glass order parameter, the overlap q , by studying its distribution function $P(q)$. In the absence of a phase transition we would be in the paramagnetic phase, and $P(q)$ should be a delta function of a positive overlap q_{EA} (so in finite systems it should be Gaussian).

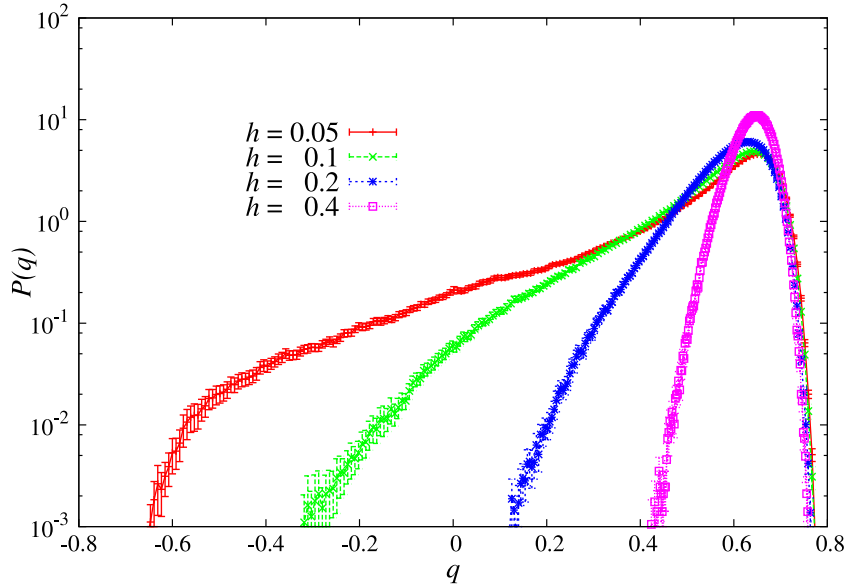


Figure 2. The probability distribution function $P(q)$ of the overlap q for our largest lattices ($L = 32$) at the lowest simulated temperature ($T = 0.805128$) for all our magnetic fields ($h = 0.05, 0.1, 0.2, 0.4$), see table 1. The order parameter in the Edwards–Anderson model is the overlap q , and it is defined in the $[-1, 1]$ interval (see section 4). The supports are wide, with exponential tails similar to those in the mean-field model at the dAT transition line [47].

Instead, we can see from figure 2 that its distribution $P(q)$ has a very wide support, with tails that, for small enough magnetic fields, even reach negative values of q . This is precisely what was observed in the mean-field version of the model on the de Almeida–Thouless line, and it was attributed to the contribution of a few samples [47].

From these arguments it becomes reasonable to think that we may not be simulating large enough lattices to observe the asymptotic nature of the system and that there may be some hidden behaviour that we are not appreciating.

2.4. Giant fluctuations

In fact, we find that the average values we measure are representative of only a small part of the data set. That is, the average of relevant observables (e.g., the spatial correlation function) only represents the small number of measurements that are dominating it. The rest of the measurements are not appreciated by using the average.

Clearly, standard finite-size scaling methods are not adequate for these systems, and we need to find a way to take *all* the measurements into account. Recalling the wide distributions of figure 2, it seems reasonable to sort our measurements according to some conditioning variable \hat{q} related to the overlaps between our replicas (see section 6). In this way, we find that the average values we measure are given by only a small part of the measurements. For example, in figure 3 we show the correlation function $C(r)$. We plot four estimators of $C(r)$: the average (which is the standard quantity studied in almost all, if not all, previous work), the $C(r)$ that corresponds to the median of the \hat{q} distribution,

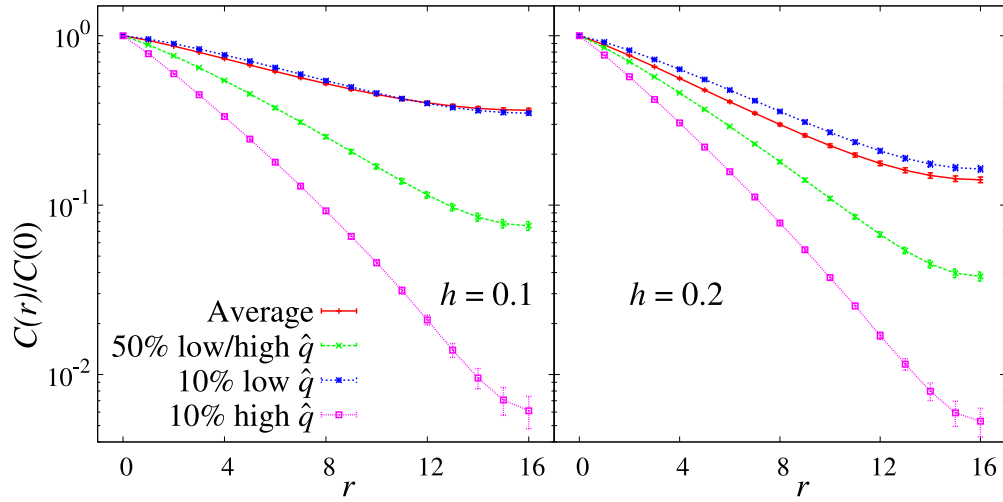


Figure 3. Different instances of the normalized correlation function $C(r)$ (9) for $L = 32$, $T = 0.805128$. The field is $h = 0.1$ on the left, and $h = 0.2$ in the right plot. We sort the measurements with the help of a conditioning variate \hat{q} as described in section 6. In this case \hat{q} is the median overlap q_{med} . We show small sets of measurements, namely the ones with the 10% lowest (top curve) and highest (bottom curve) \hat{q} and those whose \hat{q} corresponds to the median of the distribution of \hat{q} (50% lowest/highest \hat{q}). This sorting reveals extreme differences in the *fauna* of measurements. The average and median of the correlation functions are very different. The average is very similar to the 10% lowest ranked measures, i.e., it is only representative of a very small part of the data. We normalize $C(r)$ by dividing by $C(0)$ because we measure point-to-plane correlation functions (9). The correlation functions have zero slope at $r = L/2$ due to the periodic boundary conditions.

and the measurements with the 10% highest (lowest) values of \hat{q} . We see that the average is very close to the 10% lowest \hat{q} , and very far from the two other curves. Therefore, when we plot the average curve, we are only representing the behaviour of that small set of data.

Therefore, if we want to understand the behaviour of the *whole* collection of measurements, we have to be able to find some criterion to sort them and analyse them separately.

3. Model and simulations

3.1. The model

We consider a 3D cubic lattice of size L with periodic boundary conditions. In each of the $V = L^3$ vertices of the lattice there is a spin $\sigma_{\mathbf{x}} = \pm 1$. The spins interact uniquely with their nearest neighbours and with an external magnetic field h . The Hamiltonian is

$$\mathcal{H} = - \sum_{\langle \mathbf{x}, \mathbf{y} \rangle} J_{\mathbf{x}\mathbf{y}} \sigma_{\mathbf{x}} \sigma_{\mathbf{y}} - h \sum_{\mathbf{x}} \sigma_{\mathbf{x}}, \quad (1)$$

where $\langle \mathbf{x}, \mathbf{y} \rangle$ means that the sums are only over the nearest neighbours, while the couplings $J_{\mathbf{x}\mathbf{y}}$, which are constant during each simulation, take the values ± 1 with equal probability (quenched disorder). A given instance of the bonds $J_{\mathbf{x}\mathbf{y}}$ and of the intensity of the magnetic field h defines a *sample*. We will consider real *replicas* of each sample, i.e., systems with identical couplings $J_{\mathbf{x}\mathbf{y}}$ and field h , but independent evolutions (for a recent discussion see [36, 59]). In this work we will use four replicas per sample.

3.2. The simulations

For all our simulations we made use of parallel tempering (PT) [60, 61]. The whole procedure was very similar to the one in [29].

The smaller lattices ($L = 6, 8, 12$) were simulated with multispin coding (C code with words of 128 bits, by means of streaming extensions) [29, 62] on the *Memento* CPU cluster at BIFI. The larger samples ($L = 16, 24, 32$) were simulated on the *Janus* dedicated computer [38].

An elementary Monte Carlo step (EMCS) consisted of one PT exchange every ten Metropolis steps for the multispin-coding samples, and one PT every ten heatbath steps for the samples simulated on *Janus*. Table 1 shows the relevant parameters of the simulations. The temperatures were equally spaced between T_{\min} and T_{\max} . The intensities of the external magnetic field we chose were $h = 0.05, 0.1, 0.2$ and 0.4 .

To check whether the samples were thermalized we measured the exponential self-correlation time of the PT random walk in temperatures τ [29, 36, 63, 64]. We required the simulations to last at least 14τ . To do so without consuming computing time on already thermalized lattices, we assigned a minimum number of EMCSs, N_{MCS}^{\min} , for all the samples, and extended by a factor $f > 1$ only the ones that did not meet the imposed thermalization criterion. In table 1 we report N_{EMCS}^{\min} , the maximum extension factor f_{\max} of the simulations, and the minimum number N_{τ}^{\min} of EMCSs in units of τ .

Equilibrium measures were taken offline over the second half of each simulation. Independently of how much the simulations were extended, we saved 16 equally time-spaced configurations and performed measures on them. We were measuring four-replica observables. Therefore, for each sample it was possible to choose quadruplets of configurations, each from a different replica, in 16^4 ways. Out of the 16^4 possibilities, we chose $N_t = 1000$ combinations randomly. In other words, each sample participated in the statistics with $N_t = 1000$ measurements.

The errors were estimated with the jackknife method.

4. Observables

For each sample we simulated four different replicas, in order to be able to compute connected correlation functions that go to zero at infinite distance. We will label replicas by using superscripts; this means that the generic quantity $\mathcal{O}^{(a)}$ belongs to the a th replica of a given sample.

We will denote by over-lines $\overline{(\dots)}$ the averages over the samples, and by brackets $\langle \dots \rangle$ the thermal averages. To make the notation less heavy we will use $E(\dots) = \overline{\langle \dots \rangle}$ to denote an average that is taken first over the thermal fluctuations and then over the samples.

Table 1. Parameters of the simulations. We report the magnetic field h , the lattice linear size L , the number of simulated samples N_{samples} , and the basic length of a simulation in elementary Monte Carlo steps $N_{\text{EMCS}}^{\text{min}}$. In each simulation we measured the exponential correlation time τ of the PT random walk in temperatures. When τ was too large to meet our thermalization requirements, we extended the length of each simulation by an extension factor f . We denote by f_{max} the greatest extension factor. We also give the minimum length of a simulation N_{τ}^{min} in units of τ . In all cases we imposed $N_{\tau}^{\text{min}} > 14$. Finally, we give the number of temperatures N_T we used for the PT, and the minimum and maximum temperatures T_{min} and T_{max} .

h	L	N_{samples}	$N_{\text{EMCS}}^{\text{min}}$	f_{max}	N_{τ}^{min}	N_T	T_{min}	T_{max}
0.05	6	25 600	1.6×10^6	1	40.0	14	0.5	1.8
0.05	8	25 600	3.2×10^6	16	40.0	14	0.5	1.8
0.05	12	25 600	3.2×10^6	16	15.6	12	0.7	1.8
0.05	16	12 800	1.28×10^7	128	20.1	24	0.6	1.75
0.05	24	6 400	1.28×10^7	110	16.0	20	0.78	1.54
0.05	32	2 400	6.4×10^7	256	14.3	30	0.805 128	1.548 72
0.1	6	25 600	1.6×10^6	4	40.0	14	0.5	1.8
0.1	8	25 600	3.2×10^6	16	40.0	14	0.5	1.8
0.1	12	25 600	3.2×10^6	16	14.4	12	0.7	1.8
0.1	16	12 800	1.28×10^7	256	27.9	24	0.6	1.75
0.1	24	3 200	1.28×10^7	4097	14.3	24	0.66	1.58
0.1	32	1 600	6.4×10^7	533	14.4	30	0.805 128	1.548 72
0.2	6	25 600	1.6×10^6	1	40.0	14	0.5	1.8
0.2	8	25 600	3.2×10^6	16	40.0	14	0.5	1.8
0.2	12	25 600	3.2×10^6	64	25.4	12	0.7	1.8
0.2	16	12 800	1.28×10^7	256	18.4	24	0.6	1.75
0.2	24	3 200	1.28×10^7	512	16.1	24	0.66	1.58
0.2	32	1 600	1.6×10^7	513	16.0	30	0.805 128	1.548 72
0.4	6	25 600	1.6×10^6	1	40.0	14	0.5	1.8
0.4	8	25 600	3.2×10^6	4	30.7	14	0.5	1.8
0.4	12	25 600	3.2×10^6	16	14.1	12	0.7	1.8
0.4	16	3 200	1.28×10^7	32	20.1	24	0.6	1.75
0.4	24	800	1.28×10^7	29	16.1	24	0.66	1.58
0.4	32	800	3.2×10^6	16	16.4	30	0.805 128	1.548 72

We define the local overlap as

$$q_{\mathbf{x}}^{(ab)} = \sigma_{\mathbf{x}}^{(a)} \sigma_{\mathbf{x}}^{(b)}, \quad (2)$$

while the total overlap is

$$q^{(ab)} = \frac{1}{V} \sum_{\mathbf{x}} q_{\mathbf{x}}^{(ab)}. \quad (3)$$

We show in appendix B that the most informative connected correlator we can construct with four replicas is the replicon propagator [5, 65]

$$G_R(\mathbf{r}) = \frac{1}{V} \sum_{\mathbf{x}} \overline{(\langle \sigma_{\mathbf{x}} \sigma_{\mathbf{x}+\mathbf{r}} \rangle - \langle \sigma_{\mathbf{x}} \rangle \langle \sigma_{\mathbf{x}+\mathbf{r}} \rangle)^2}. \quad (4)$$

To compute G_R we calculate the four-replica field

$$\Phi_{\mathbf{x}}^{(ab;cd)} = \frac{1}{2}(\sigma_{\mathbf{x}}^{(a)} - \sigma_{\mathbf{x}}^{(b)})(\sigma_{\mathbf{x}}^{(c)} - \sigma_{\mathbf{x}}^{(d)}), \quad (5)$$

where the indices a, b, c, d indicate strictly different replicas. Notice that

$$\left\langle \Phi_{\mathbf{x}}^{(ab;cd)} \Phi_{\mathbf{y}}^{(ab;cd)} \right\rangle = (\langle \sigma_{\mathbf{x}} \sigma_{\mathbf{x}+\mathbf{r}} \rangle - \langle \sigma_{\mathbf{x}} \rangle \langle \sigma_{\mathbf{x}+\mathbf{r}} \rangle)^2, \quad (6)$$

so we obtain G_R by also taking the average over the samples

$$E(\Phi_{\mathbf{x}}^{(ab;cd)} \Phi_{\mathbf{y}}^{(ab;cd)}) = G_R(\mathbf{x} - \mathbf{y}). \quad (7)$$

Here and everywhere there is more than one possible permutation of the replica indices; we average over all of them to gain statistics.

Correlations in the Fourier space are defined analogously, by Fourier-transforming $\Phi_{\mathbf{x}}^{(ab;cd)}$, so the wavevector dependent replicon susceptibility is expressed as

$$\chi_R(\mathbf{k}) = \frac{1}{V} E(|\hat{\Phi}_{\mathbf{k}}^{(ab;cd)}|^2), \quad \hat{\Phi}_{\mathbf{k}}^{(ab;cd)} = \sum_{\mathbf{x}} e^{i\mathbf{k}\cdot\mathbf{x}} \Phi_{\mathbf{x}}^{(ab;cd)}. \quad (8)$$

When we omit \mathbf{k} , we refer to the susceptibility $\chi = \chi_R(\mathbf{0})$.

We compute point-to-plane correlation functions

$$C(r) = \frac{1}{L} \sum_{n=0}^{L-1} e^{-ir2\pi n/L} \chi_R\left(\frac{2\pi n}{L}, 0, 0\right) \equiv \sum_{y,z} G_R(x=r, y, z). \quad (9)$$

The previous relation is equivalent if we align the wavevector along any of the three coordinate axes, so we average over these three choices.

With the defined observables we were able to calculate the second-moment correlation length

$$\xi_L = \frac{1}{2 \sin(k_{\min}/2)} \sqrt{\frac{\chi_R(\mathbf{0})}{\chi_R(2\pi/L, 0, 0)} - 1} \quad (10)$$

and the dimensionless quantity

$$R_{12} = \frac{\chi_R(2\pi/L, 0, 0)}{\chi_R(2\pi/L, \pm 2\pi/L, 0)}, \quad (11)$$

where all the quantities were averaged over all the possible permutations of the components of the wavevectors.

The cumulant R_{12} (recall figure 1) was used in [29] to estimate the critical temperature bypassing pathologies on $\chi(\mathbf{0})$ due to the fact that the overlap is non-zero in the paramagnetic phase (recall figure 2).

5. Finite-size scaling

Our finite-size scaling analysis follows phenomenological renormalization, which is very effective when one looks for a phase transition with a diverging correlation length [66, 48, 67]. In fact, under the accepted assumption that there is only one relevant length scale in the system, close to the critical temperature T_c a generic observable \mathcal{O} scales as

$$\langle \mathcal{O}(L, T) \rangle = L^{x_{\mathcal{O}}/\nu} \left[\mathcal{F}_{\mathcal{O}}(L^{1/\nu}(T - T_c)) + O(L^{-\omega}) \right], \quad (12)$$

where $\omega > 0$ represents the leading irrelevant exponent.

This implies that at the critical point the quantities $\xi_L(T, L, h)/L$ and $R_{12}(T, L, h)$ are scale invariant to the dominant order,

$$\frac{\xi_L}{L}(L, T) = \mathcal{F}_{\xi}(L^{1/\nu}(T - T_c)) + \dots, \quad (13)$$

$$R_{12}(L, T) = \mathcal{F}_R(L^{1/\nu}(T - T_c)) + \dots, \quad (14)$$

where the dots indicate subleading corrections to scaling. Therefore, for large enough systems the critical point at given h would be revealed by the crossing points of these curves for different sizes. As figure 1 shows, such a crossing is not present in our data.

With the use of the hyperscaling relations we can also predict the scaling of the susceptibility close to the critical point,

$$\chi_R(L, T) = L^{2-\eta} \mathcal{F}_{\chi}(L^{1/\nu}(T - T_c)) + \dots. \quad (15)$$

6. Conditional expectation values and variances

6.1. The conditioning variate

As we pointed out in section 2, the behaviour of the system is dominated by a very small number of measurements.

This means that the average over all the measurements of an observable does not describe the typical behaviour of the system. Furthermore, the behaviour of the measurements that contribute less to the full averages is qualitatively different from the behaviour of those that give the main contribution (see figure 3 and section 8 below).

We want to classify our measurements in a convenient way, in order to be able to separate different behaviours, and analyse them separately. To this end, we replace the normal expectation value $E(\mathcal{O})$ of a generic observable \mathcal{O} with the expectation value $E(\mathcal{O}|\hat{q})$ conditioned to another random variable \hat{q} . Perhaps due to lack of imagination \hat{q} will be called the conditioning variate. For each instance of \mathcal{O} we monitor also the value of \hat{q} , and we use it to label \mathcal{O} . Hopefully, there will be some correlation.

The conditional expectation value is defined as the average of \mathcal{O} , restricted to the measurements i (out of the $\mathcal{N}_m = N_t N_{\text{samples}}$ total measurements) that simultaneously yield \mathcal{O}_i and \hat{q}_i (so we are actually talking about couples of simultaneous measurements $(\mathcal{O}_i, \hat{q}_i)$) in a small interval around $\hat{q} = c$,

$$E(\mathcal{O}|\hat{q} = c) = \frac{E[\mathcal{O}_i \mathcal{X}_{\hat{q}=c}(\hat{q}_i)]}{E[\mathcal{X}_{\hat{q}=c}(\hat{q}_i)]}, \quad (16)$$

where we have used the characteristic function

$$\mathcal{X}_c(\hat{q}_i) = \begin{cases} 1, & \text{if } |c - \hat{q}_i| < \epsilon \sim \frac{1}{\sqrt{V}}, \\ 0, & \text{otherwise.} \end{cases} \quad (17)$$

In appendix C we give technical details on the choice of ϵ . To make the notation lighter, in the rest of the paper we will replace $E(\mathcal{O}|\hat{q} = c)$ with $E(\mathcal{O}|\hat{q})$.

The traditional expectation value $E(\mathcal{O})$ can be recovered by integrating over all the possible values of the conditioning variate \hat{q} ,

$$E(\mathcal{O}) = \int d\hat{q} E(\mathcal{O}|\hat{q})P(\hat{q}), \quad P(\hat{q}) = E[\mathcal{X}_{\hat{q}}], \quad (18)$$

where $P(\hat{q})$ is the probability distribution function of the conditioning variate.

We remark that the concept of conditioning variate is fairly similar to that of control variate. However, the latter was formalized slightly differently, and with the objective of enhancing the precision of the measures [68]. In [36, 69] a procedure very similar to the present one was followed, but the aim was the construction of clustering correlation functions, while in our case the conditioning variate is used to analyse *separately* different behaviours coming from the same global data set, so that a sensible finite-size scaling becomes possible.

6.2. Measurements against samples

The reader may argue that a sample-to-sample distinction of the different behaviours is more natural than a measurement-dependent one (although intuition leads one to assume that the two are related). This was indeed our first approach to the problem (it was, in fact, proposed in [47]). However, we found that the approach described in the previous section is preferable, for both practical and conceptual reasons.

On the practical side, a sample-to-sample separation implies that from each sample we get only one data point: for any observable, we limit ourselves to its thermal average. In this case we would need a limitless number of samples to be able to construct a reasonable $P(\hat{q})$. Moreover, the simulations should last a huge number of autocorrelation times τ if we want to have small enough errors in the thermal averages of each sample. Otherwise, we would introduce a large bias that is not reduced on increasing the number of samples.

On the conceptual side, representation of each sample merely with a single number (namely the thermal expectation value) is a severe oversimplification. As we show in figure 4, even though we are in the paramagnetic phase, the behaviour within each sample is far from trivial. For a non-negligible fraction of the samples, the overlap distribution is wide, often with a multi-peak structure. The barriers among peaks can be deep, hence suggesting extremely slow dynamics (which is indeed the case for physical dynamics [34] or for the parallel-tempering dynamics, see section 3).

In summary, we find that the use of instantaneous measurements to classify the available information is the best solution.

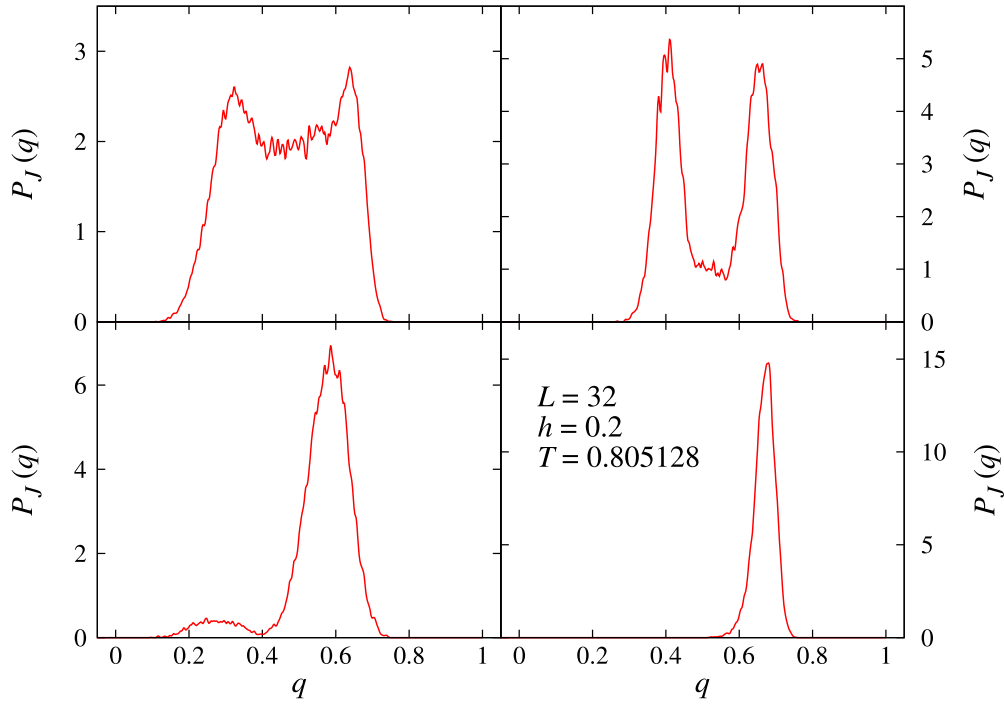


Figure 4. Sample-dependent probability distribution functions $P_J(q)$, for four different samples, each representing a different type of $P_J(q)$ we encountered. As well as the averaged $P(q)$, the sample-dependent density function can also be wide and have a structure. The plotted data come from samples with $L = 32$, $h = 0.2$ and $T = 0.805128$.

6.3. The selection of the conditioning variate

6.3.1. A quantitative criterion. A convenient conditioning variate is the one that mostly discerns the different behaviours of the model. We can obtain a quantitative criterion for the selection of a good \hat{q} by examining the following relation for any conditional variance:

$$\text{var}(\mathcal{O}) = c_1 + c_2, \quad (19)$$

where we defined

$$\begin{aligned} c_1 &\equiv \int_{-1}^1 d\hat{q} P(\hat{q}) \text{var}(\mathcal{O}|\hat{q}), & \text{var}(\mathcal{O}|\hat{q}) &= E([\mathcal{O} - E(\mathcal{O}|\hat{q})]^2|\hat{q}), \\ c_2 &\equiv \int_{-1}^1 d\hat{q} P(\hat{q}) [E(\mathcal{O}) - E(\mathcal{O}|\hat{q})]^2. \end{aligned} \quad (20)$$

Both c_1 and c_2 are positive, and their sum is fixed.

Let us explain intuitively why a useful conditioning variate has $c_2 \gg c_1$.

If $c_1 = 0$ the fluctuations of \mathcal{O} would be explained solely by the fluctuations of \hat{q} . In this case c_2 is large and assumes its largest possible value, meaning that different values of \mathcal{O} are mostly spread apart by \hat{q} .

On the other hand, $c_2 = 0$ implies $E(\mathcal{O}) = E(\mathcal{O}|\hat{q})$ and signals an insensitive conditioning variate, with null correlation between \mathcal{O} and \hat{q} .

Equations (19) and (20) can thus be used to quantify the quality of the conditioning variate \hat{q} : we look for the highest quotient c_2/c_1 .

6.3.2. Candidates for \hat{q} . To select an appropriate conditioning variate we need to choose \mathcal{O} and propose some test definitions for \hat{q} . The functions of the observables that one could use as a conditioning variate are infinite, but physical intuition leads us to try with simple functions of the overlap. On the other hand, a natural choice of \mathcal{O} is the estimator of the replicon susceptibility (see (8)). This means that

$$\mathcal{O} \longrightarrow \frac{1}{3\mathcal{N}} \sum_{\substack{\text{equiv. wave} \\ \text{vectors } \mathbf{k}}}^{\mathcal{N}} \left[|\Phi_{\mathbf{k}}^{(ab;cd)}|^2 + |\Phi_{\mathbf{k}}^{(ac;bd)}|^2 + |\Phi_{\mathbf{k}}^{(ad;bc)}|^2 \right], \quad (21)$$

where \mathcal{N} is the number of equivalent wavevectors one can construct. This is a four-replica quantity (see (4)), so six instantaneous overlaps are associated with each instance of the correlators. To define \hat{q} we need to propose a function of the six overlaps in order to get a one-to-one correspondence.

Let us reorder each six-plet of instantaneous overlaps $\{q^{(ij)}\}$ in the form of six sorted overlaps $\{q_k\}$,

$$\left\{ q^{(ab)}, q^{(ac)}, q^{(ad)}, q^{(bc)}, q^{(bd)}, q^{(cd)} \right\} \longrightarrow \{q_1 \leq q_2 \leq q_3 \leq q_4 \leq q_5 \leq q_6\}. \quad (22)$$

The following are natural test conditioning variates:

$$\hat{q} = \begin{cases} q_{\min} = q_1 & \text{(the minimum),} \\ q_{\max} = q_6 & \text{(the maximum),} \\ q_{\text{med}} = \frac{1}{2}(q_3 + q_4) & \text{(the median),} \\ q_{\text{av}} = \frac{1}{6}(q_1 + q_2 + q_3 + q_4 + q_5 + q_6) & \text{(the average).} \end{cases} \quad (23)$$

Table 2 depicts the c_1 and c_2 terms, and their ratio, for all the conditioning variates, for a single triplet (T, L, h) and $\mathbf{k} = (0, 0, 0)$. The best conditioning variate is clearly the median, since it has the highest c_2/c_1 ratio. The situation is similar for other choices of (T, L, h) .

For a qualitative description of the difference between the diverse conditioning variates, in figure 5 (top) the reader can appreciate the probability distribution functions for each of the conditioning variates, while in figure 5 (bottom) we plotted the conditional susceptibilities. From (18) we stress that the integral of the values on the top times the values of the bottom set yields the average susceptibility, which is indicated with a horizontal line on the bottom plot of figure 5. As is also reflected by table 2, q_{\max} is the worst conditioning variate, as its χ does not vary much with the fluctuations of q_{\max} . The steepest slope is obtained when the conditioning variate is q_{av} or q_{med} , but the latter is smoother and covers a wider range of χ .

Figure 5 also displays the large deviations present in the system. In fact, one can see that the value of q_{med} at which $P(q_{\text{med}})$ has its maximum is significantly different with respect to the value of q_{med} at which $\chi(q_{\text{med}})$ assumes the value of the average.

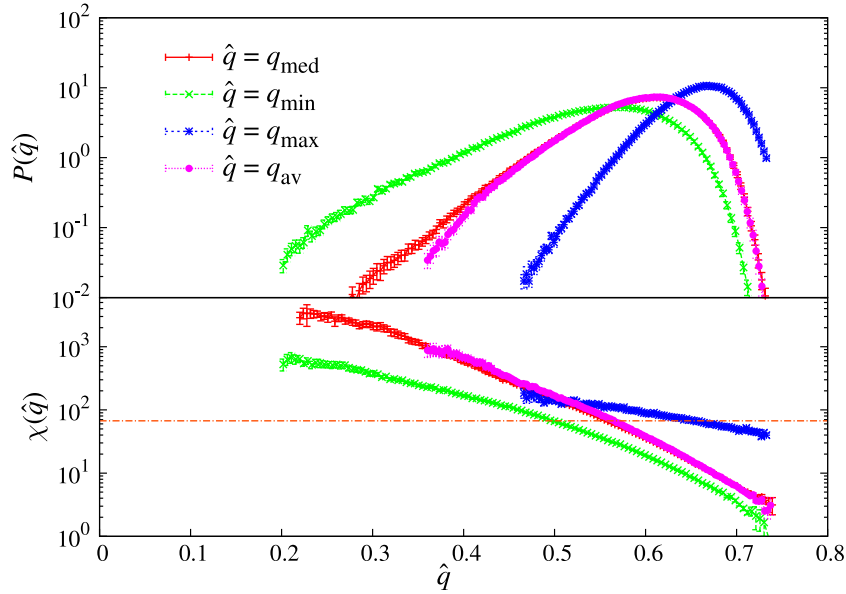


Figure 5. Features of the diverse conditioning variates we proposed for $L = 32$, $h = 0.2$ and $T = 0.805\,128$. The top figure shows the histograms $P(\hat{q})$ for our four candidates for the conditioning variate: the minimum overlap q_{\min} (of the six we can make with four replicas, recall (23)), the maximum q_{\max} , the median q_{med} and the average q_{av} . The histograms were constructed as explained in appendix C. The bottom figure depicts the size of the susceptibility χ for each value of the conditioning variate. The horizontal line marks the value of χ when it is averaged over the full set of measurements. For aesthetic reasons in both figures we have cut the curves at the two end points, where they become extremely noisy due to poor sampling.

Table 2. Criterion for the choice of the conditioning variate \hat{q} for $h = 0.1$, $L = 32$, $T = 0.805\,128$, by looking at the indicators c_1 and c_2 relative to $\chi_{\text{R}}(\mathbf{0})$. We want the \hat{q} to split the different measured susceptibilities as much as possible. This is realized, see (20), when the ratio c_2/c_1 is maximized. From the data we see that this occurs with $\hat{q} = q_{\text{med}}$.

\hat{q}	c_1	c_2	c_2/c_1
q_{\min}	$399\,000 \pm 37\,000$	$121\,000 \pm 15\,000$	0.30(6)
q_{\max}	$514\,000 \pm 51\,000$	$6\,230 \pm 690$	0.012(3)
q_{med}	$162\,000 \pm 10\,000$	$358\,000 \pm 45\,000$	2.2(4)
q_{av}	$328\,000 \pm 26\,000$	$192\,000 \pm 28\,000$	0.6(1)

7. Quantiles and a modified finite-size scaling ansatz

We stated in section 2 that the set of measurements with low \hat{q} has a very different behaviour from the measurements with high \hat{q} (recall figure 3). From now on, we shall restrict ourselves to $\hat{q} = q_{\text{med}}$, since we evinced that the median is our best conditioning

variate. Our next goal will be to carry out a finite-size scaling analysis based on the $P(q_{\text{med}})$ that lets us observe different parts of the spectrum of behaviours of the system.

In order to analyse these different sets of measures separately, we divide the $P(q_{\text{med}})$ into ten sectors, each containing 10% of the measured q_{med} . We focus our analysis on the values of q_{med} that separate each of these sectors. They are called quantiles (see, e.g., [70]), and we label them with the subscript $i = 1, \dots, 9$. If we denote by $\tilde{q}_i(h, T, L)$ the value of the i th quantile, we can define it in the following implicit way:

$$\int_{-1}^{\tilde{q}_i} d\hat{q} P(\hat{q}) = \frac{i}{10}. \quad (24)$$

In appendix C we explain how $\tilde{q}_i(h, T, L)$ was computed.

We can adapt the definitions we gave in section 4 to the i th quantile,

$$\chi_{R,i}(\mathbf{k}) = \frac{1}{V} E \left(|\hat{\Phi}_{\mathbf{k}}^{(ab;cd)}|^2 \mid \tilde{q}_i \right), \quad (25)$$

$$\xi_{L,i} = \frac{1}{2 \sin(k_{\text{min}}/2)} \sqrt{\frac{\chi_{R,i}(\mathbf{0})}{\chi_{R,i}(2\pi/L, 0, 0)} - 1}, \quad (26)$$

$$R_{12,i} = \frac{\chi_{R,i}(2\pi/L, 0, 0)}{\chi_{R,i}(2\pi/L, \pm 2\pi/L, 0)}. \quad (27)$$

In this way we can extend the finite-size scaling methodology to the i th quantile,

$$\frac{\xi_L}{L} \Big|_{T,h,L,i} = \mathcal{F}_{\xi_i} \left(L^{1/\nu} (T - T_c) \right), \quad R_{12} \Big|_{T,h,L,i} = \mathcal{F}_{R_i} \left(L^{1/\nu} (T - T_c) \right). \quad (28)$$

This is a new approach for finite-size scaling. Although it demands a very large amount of data because it is carried out over a small fraction of the measurements, it allows us to perform finite-size scaling on selected sets of measurements. Let us stress that no *a priori* knowledge is required on the probability distribution function $P(q_{\text{med}})$: quantiles are conceived in order to define a scaling that self-adapts when the volume increases. In section A.2 we show the validity of this ansatz in zero field.

7.1. The $P(q_{\text{med}})$

To the best of our knowledge, despite its simplicity the median overlap q_{med} has not been studied before. In fact, we just lacked the motivation to investigate its features. However, we now base our analysis on this quantity, so we feel that it is necessary to dedicate a section to it.

By its definition, the probability distribution $P(q_{\text{med}})$ of the median overlap has narrower tails than $P(q)$ (recall figure 2), although from figure 5 (top) it is clear that the strong fluctuations persist also with q_{med} .

The median of $P(q_{\text{med}})$ corresponds to the fifth quantile. We prefer to call it the ‘fifth quantile’ rather than the ‘median of the median overlap’. Of the nine studied quantiles it is the smoothest and has the least finite-size effects, as one can see from figure 6 (inset). Further analysis is given in appendix E.

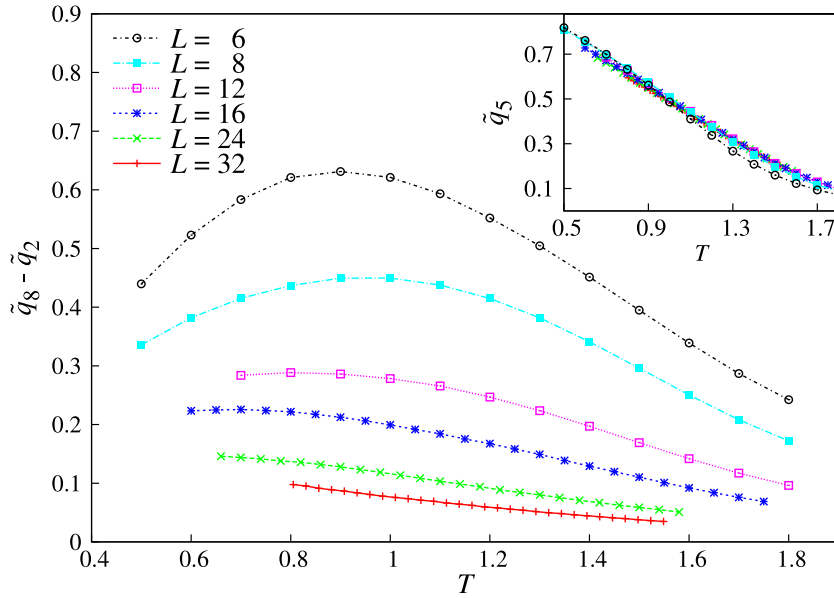


Figure 6. Using q_{med} as the conditioning variate, we show the temperature dependence of the difference between quantiles $\tilde{q}_8 - \tilde{q}_2$, for all our lattice sizes, in a field of intensity $h = 0.2$. This corresponds to the width of the central 60% of the area of $P(q_{\text{med}})$. This quantity can reveal a phase transition, since in the paramagnetic phase the $P(q_{\text{med}})$ should be a delta function, while in the spin-glass phase it should have a finite support. We show the central 60% and not a wider range because it is an equivalent indicator of the phase transition, and it is safer from rare events that would vanish in the thermodynamic limit. In the inset we show the position of the fifth quantile as a function of temperature for all our lattice sizes. It is a very smooth curve with very small finite-size effects.

We remark also that the separation between the different \tilde{q}_i s can be used as an order parameter, since its thermodynamic limit should be zero in the paramagnetic phase, and greater than zero in the possible low-temperature phase due to the (would-be) replica symmetry breaking. Figure 6 shows the difference between the eighth and the second quantile, i.e., the q_{med} -span of the central 60% of the data. If we were able to extrapolate a clean $L \rightarrow \infty$ limit for this curve, we would be able to answer the question of whether the transition exists or not. Unfortunately, even for $T > T_c(h = 0) = 1.1019(29)$, where we know that we are in the paramagnetic phase, it is not possible to make good extrapolations since the trend is strongly non-linear. In appendix E we show that extrapolations to the thermodynamic limit were only possible in the trivial case of $h = 0.4$ (deep paramagnetic phase), and that amongst all the quantiles, the median curve is the one that shows the least finite-size effects.

8. Results

As already stressed, the behaviour of the system is characterized by very strong fluctuations, and a wide and asymmetric $P(q)$. As a result, the average and median

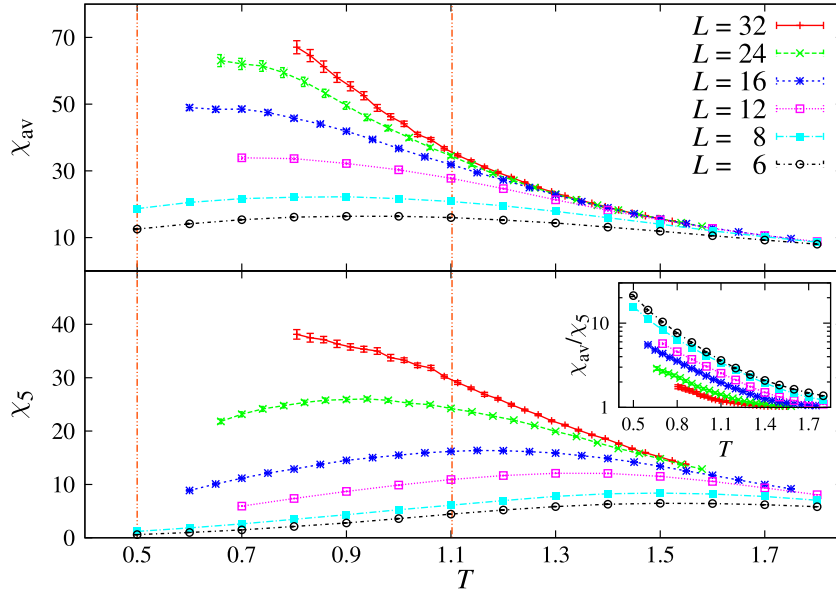


Figure 7. The replicon susceptibility χ as a function of the temperature, for all the simulated lattice sizes and the field $h = 0.2$. We represent its average χ (top) and the fifth quantile χ_5 with $\hat{q} = q_{\text{med}}$ (bottom). In both plots, the two vertical lines represent the upper bound of the possible phase transition $T^{\text{up}}(h = 0.2) = 0.5$ [34] and the zero-field critical temperature $T_c(h = 0) = 1.109(29)$ [51]. The amplitudes and the positions of the peaks of χ are strikingly different (note the different scales on the y axes). The inset shows the ratio between the two, which we expect to tend to an order-one constant in the thermodynamic limit. This is actually what we see at high temperatures.

behaviours are very different. In figure 7, we show the replicon susceptibility, its average χ on the left plot, and its fifth quantile χ_5 . Motivated by the arguments in section 6, all the quantiles we show in this section use the conditioning variate $\hat{q} = q_{\text{med}}$.

Visibly, not only is the average susceptibility much larger than the fifth quantile, but also the two have peaks at different temperatures. Also, finite-size effects are much stronger in the case of χ_5 (yet, recall the inset in figure 6, finite-size effects on \tilde{q}_5 are tiny)¹⁴.

We show in figure 8 how sorting the data with the quantiles revealed the presence of different types of behaviour, by plotting the ξ_L/L and the R_{12} for quantiles 1, 5 and 9 at $h = 0.2$.¹⁵ There are two vertical lines in each figure. The one on the left represents the upper bound $T^{\text{up}}(h)$ for the phase transition (meaning that no phase transition can occur for $T > T^{\text{up}}(h)$) given in [34], while the one on the right indicates the zero-field critical temperature $T_c = 1.1019(29)$ [51].

We can see that the first quantile has the same qualitative behaviour of the average (figure 1), but lower values, since the main contribution to the average comes from data

¹⁴ We made power law extrapolations to $L \rightarrow \infty$ of the maxima of the susceptibility, but they were not satisfactory (too large a value of χ^2/DOF). Only for $h = 0.2, 0.4$ were we able to fit the heights of the maxima and we obtained $\eta(h = 0.2) \approx 0.6$ and $\eta(h = 0.4) \approx 0.9$.

¹⁵ In section A.1 we show the same plots for $h = 0.1$, and in section A.2 we validate our method in the null-field case, where it is known that there actually is a phase transition.

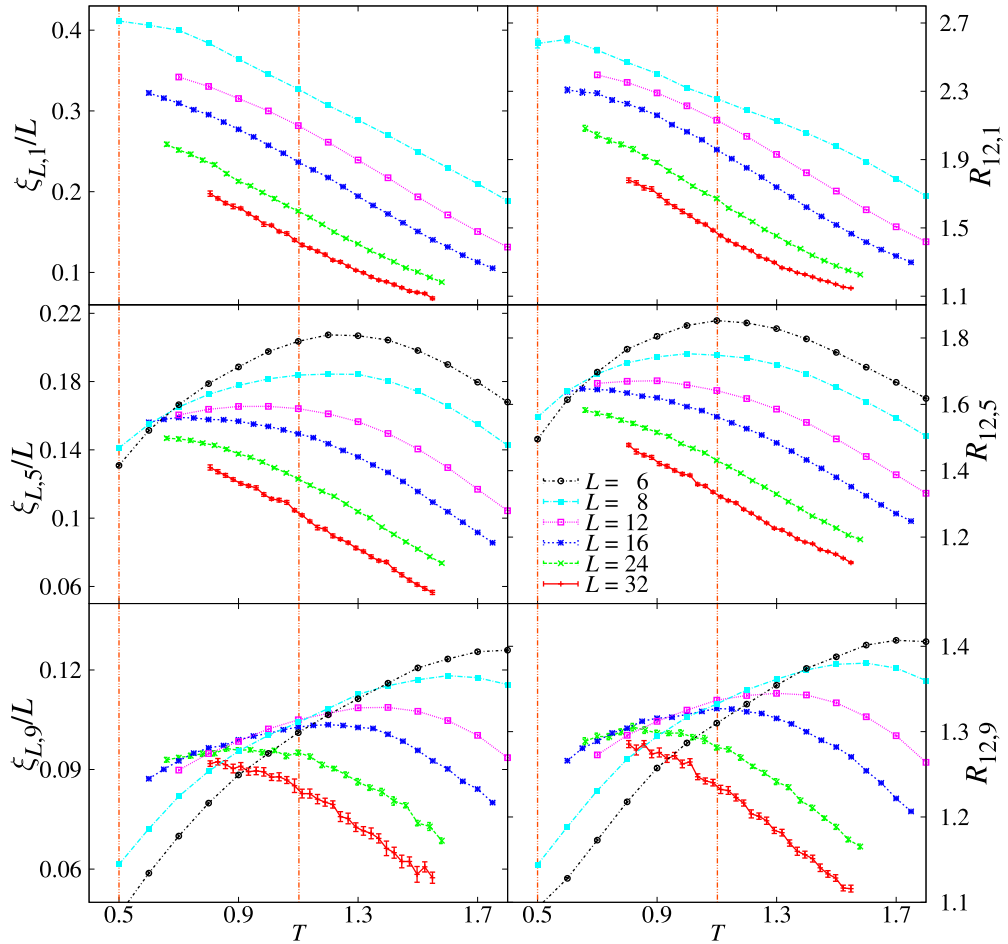


Figure 8. Finite-size indicators of a phase transition, computed for $h = 0.2$. On the left side we plot, for quantiles 1 (top), 5 (middle) and 9 (bottom), the correlation length in units of the lattice size ξ_L/L (left) versus the temperature, for all our lattice sizes except $L = 6$ (we show in appendix D that the quantile description is not suitable for $L = 6$ because there is a double peak in the $P(q)$). On the right we show analogous plots for R_{12} . The vertical line on the left marks the upper bound T^{up} for a possible phase transition given in [34], while the one on the right marks the zero-field transition temperature T_c given in [51]. Quantile 1 has the same qualitative behaviour of the average ξ_L/L , shown in figure 1, while quantiles 5 and 9 suggest a scale invariance at some temperature $T_h < T^{\text{up}}$.

whose q_{med} is even lower than \tilde{q}_1 . Moreover, one can notice that in figure 1 the indicators ξ_L/L and R_{12} show a different qualitative behaviour when the lattices are small (R_{12} shows a crossing). This discrepancy vanishes when we look only at the first quantile: separation of the different behaviours enhances the consistency between ξ_L/L and R_{12} .

The behaviour of the fifth quantile is quite different, since now it appears reasonable that the curves cross at some $T \lesssim T^{\text{up}}(h)$. The crossings become even more evident when we consider the highest quantile.

All this is consistent with the arguments of section 2, where we showed how the correlation function is dominated by a small portion of the data, near the first quantile (figure 3), while the behaviour of the majority of the samples is hidden.

Unfortunately, the high non-linearity of the curves impedes an extrapolation of the crossing points, but they are apparently compatible with the upper bound T^{up} , and their heights apparently do not depend on the intensity of the applied field h (appendix A).

9. This is not an echo of the $h = 0$ transition

The crossing suggested by the quantiles 5 and 9 in figure 8 is unlikely to be caused by the zero-field transition, since it appears at $T < T_c$ and shifts towards lower temperatures as the lattice size increases. Also, the value of ξ_L/L (R_{12}) at the possible crossing point of the fifth quantile is upper-bounded to $\xi_L/L \simeq 0.16$ ($R_{12} \simeq 1.65$), while for $h = 0$ it is considerably larger ($\xi_L(T_c)/L \simeq 0.28$ ($R_{12}(T_c) \simeq 2.15$)), see section A.2. In this section we will give more arguments supporting that what is seen is not an effect of the zero-field transition.

9.1. An escaping transition

As was pointed out in section 2, there is a controversy because we observe a wide $P(q)$, just like in the mean-field model, but the curves $\xi_L/L(T)$ and $R_{12}(T)$ do not show any sign of a crossing. If we were in the presence of a phase transition, a straightforward explanation could reside in an anomalous exponent η close to 2 [52], since at the critical temperature the replicon susceptibility scales as $\chi_R(L) \sim L^{2-\eta}$ (15). It is possible to calculate η with the quotient method [48, 67], by comparing the susceptibilities of different lattice sizes at the critical point T^* ,

$$\frac{\chi_{2L}(T^*)}{\chi_L(T^*)} = 2^{2-\eta} + \dots, \quad (29)$$

where the dots stand for subleading terms. This definition only makes sense at criticality, but we can extend it in an effective manner to a generic temperature. In this way we can delineate an effective exponent

$$\eta_{\text{eff}}(T; L, 2L) = 2 - \log_2 \frac{\chi_{2L}(T)}{\chi_L(T)}. \quad (30)$$

If there were a phase transition at a finite temperature T_h , we would have $\eta_{\text{eff}}(T_h) = \eta$. We should have $\eta_{\text{eff}} = 2$ in the paramagnetic phase, $\eta_{\text{eff}} = -1$ in the deep spin-glass phase (see section B.1, keeping in mind that $\eta_{\text{eff}} = -1$ is somewhat trivial in the limit $h \rightarrow 0$, where χ reduces to $\chi = VE(q^2)$) and signs of a crossing at $\eta_{\text{eff}} = \eta(h = 0) = -0.3900(36)$ [51] in the limit of a complete domination by the $h = 0$ transition.

In figure 9 we show $\eta_{\text{eff}}(T)$ for $h = 0.4$, $h = 0.1$ and $h = 0$ (the $h = 0$ data come from the simulations we performed in [51])¹⁶. If a phase transition were present, but hidden by heavy finite-size effects, we would expect at least that the L -trend of η_{eff} would be

¹⁶ For each jackknife block we calculated $\eta_{\text{eff}}(T)$ and made a cubic spline temperature interpolation.

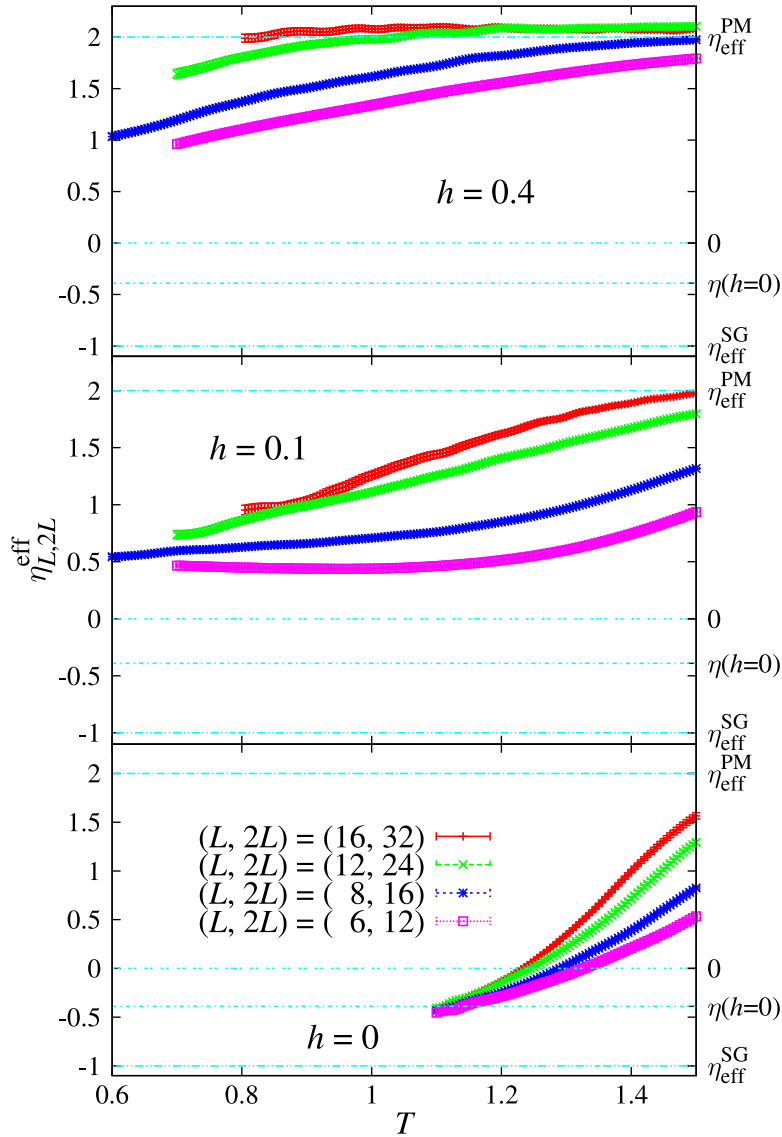


Figure 9. A plot of $\eta_{\text{eff}}(T)$, defined in (30), for all the pairs $(L, 2L)$ we could form. The magnetic fields are $h = 0.4$ (top), $h = 0.1$ (centre) and $h = 0$ (bottom). The $h = 0$ data come from [51]. In each plot we use horizontal lines to underline meaningful limits, and we label them with a tick on the right axis. From top to bottom, we depict the limit $\eta_{\text{eff}}^{\text{PM}} = 2$ of a system in the paramagnetic phase, the $\eta_{\text{eff}} = 0$ axis, the zero-field value $\eta_{\text{eff}}(h = 0, T_c) = -0.3900(36)$ [51] and its value in a deep spin-glass phase $\eta_{\text{eff}}^{\text{SG}} = -1$. Notice the difference between the case with or without a field. For $h = 0.1$ the curves appear to converge to a positive $\eta_{\text{eff}} \simeq 0.5$, while in the latter case all the curves become negative and merge at $\eta_{\text{eff}}(h = 0, T_c)$.

decreasing. In contrast, the larger our lattices are, the wider the temperature range in which $\eta_{\text{eff}} = 2$ is. The apparent phase transition shifts towards lower temperature when we suppress finite-size effects. The data in our possession are not sufficient to state whether

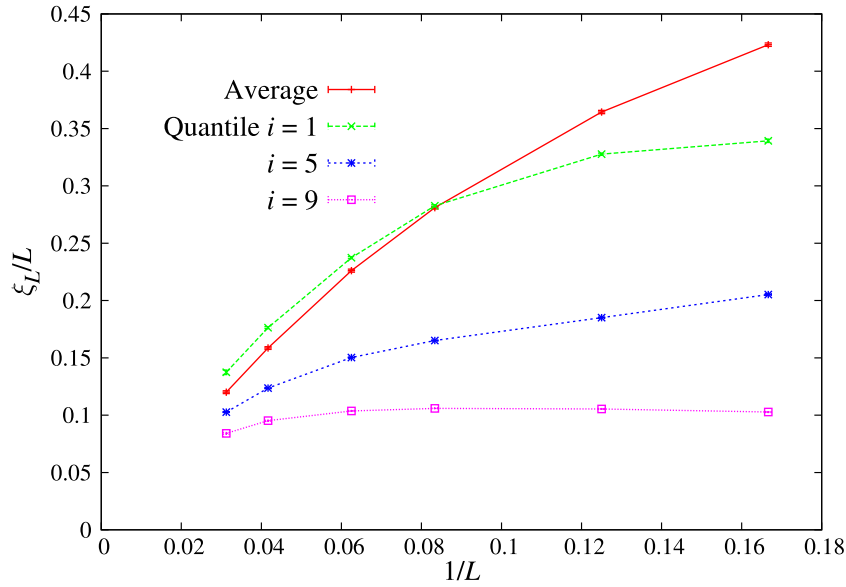


Figure 10. The scaling of ξ_L/L at the null-field critical temperature $T_c = 1.109(29)$ [51], with $h = 0.2$. We show the behaviour of the average and of quantiles 1, 5 and 9. If L is large enough, ξ_L/L should go as $1/L$, while if the system is seeing purely an echo of the divergence of the $h = 0$ transition, then ξ_L/L should be constant.

this shift will converge to a positive temperature. In any case, this is compatible with the upper bounds to a possible transition given in [34].

On the other hand, η_{eff} stays positive for all our simulated lattices (except $h = 0.05$, $L = 6$), and even for $T < T_c(h = 0)$ it tends to some value around 0.5, so it is unlikely that the null-field transition is dominating the behaviour of the system.

9.2. Scaling at $T = T_c(h = 0)$

From the scaling with the lattice linear size of ξ_L/L at $T_c = T_c(h = 0)$, we can obtain another element to discard the hypothesis that the $h = 0$ transition is biasing our measures significantly. Assuming that there is no critical line for $h > 0$, a very large correlation length could be due to an echo of the zero-field transition or a low-temperature effect. In a theory that predicts that the system is critical only at $h = 0$, $T = T_c$, the effects of this echo on the $h > 0$ behaviour should be maximal near $T = T_c$. Therefore, if we find a ξ that is large compared with our lattice sizes for $T < T_c$, a primary check is to monitor the scaling of the coherence length at T_c . Figure 10 shows the scaling of ξ_L/L at T_c with $h = 0.2$. We plot the average, the first, the fifth and the highest quantile. All of them show a clear decrease of ξ_L/L on increasing the lattice size, so our lattice sizes are large enough to state that the divergence at $h = 0$ is not dominating the behaviour of ξ_L . On the other hand, we are still far from the thermodynamic limit, since when the lattices are large enough, $\xi_L(T_c)/L$ should decay to zero linearly in $1/L$.

10. Conclusions

We have studied the equilibrium behaviour of the three-dimensional Ising Edwards–Anderson spin glass in an external magnetic field. Thermalization of the system at sufficiently low temperature was a computationally hard task and required the use of the *Janus* dedicated computer to thermalize lattice sizes up to $L = 32$, down to temperatures $T \geq 0.8$.

First of all, we carried out a traditional analysis of our data. We chose observables that would be scale invariant at the critical temperature, and compared them for different lattice sizes, looking for crossings in their temperature curves. With this procedure we found no traces of a phase transition.

However, the scenario is more complicated. Despite the absence of crossings, indications that something non-trivial is going on are given by signals such as a growing correlation length (even for our largest lattices), peaks in the susceptibility, and a wide probability distribution function of the overlap.

We noticed a wide variety of behaviours within the same set of simulation parameters. Some measurements presented signs of criticality while others did not. Therefore, we tried to classify them in a meaningful way. We sorted our observables with the help of a conditioning variate, and came up with a quantitative criterion to select the best conditioning variate. Amongst the ones we proposed, the function of the instant overlaps that made the best conditioning variate turned out to be the median overlap q_{med} .

As a function of the median overlap, the scenario appeared rather non-trivial. The averages turned out to be dominated by a very small number of measurements. Those with a small q_{med} behaved similarly to the average: long correlation lengths, very large susceptibilities and no signs of criticality. On the other hand, the median behaviour was far from the average, and the behaviour of most of the measurements was qualitatively different from the average, with smaller correlation lengths and susceptibilities, but non-negligible indications of scale invariance right below the upper bound $T^{\text{up}}(h)$ given in [34]. Furthermore, by separating the different behaviours of the system we obtained mutually consistent indications of criticality from our primary dimensionless magnitudes $\xi_{L,i}/L$ and $R_{12,i}$. The achievement of this consistency is an important step forward with respect to [29], where the phase transition was revealed only by the R_{12} indicator, but was invisible to ξ_L/L .

Unfortunately, we were not able to make a quantitative prediction of the critical temperatures $T_c(h)$, because the observables as a function of the lattice size and the temperature were very non-linear, and the temperatures we reached were not low enough to reliably identify the crossing points of the quantile-dependent $\xi_{L,i}/L$ and $R_{12,i}$.

Overall, the presence of a phase transition appears plausible from our simulations (see also appendix G). Perhaps more importantly, the challenge is now well defined: in order to be able to give, numerically, a conclusive answer on the presence of a de Almeida–Thouless line we need push our simulations down to $T \simeq 0.4$ (at $h = 0.2$). We believe that *Janus II*, the next generation of our dedicated computer [34], will be able to assume this challenge.

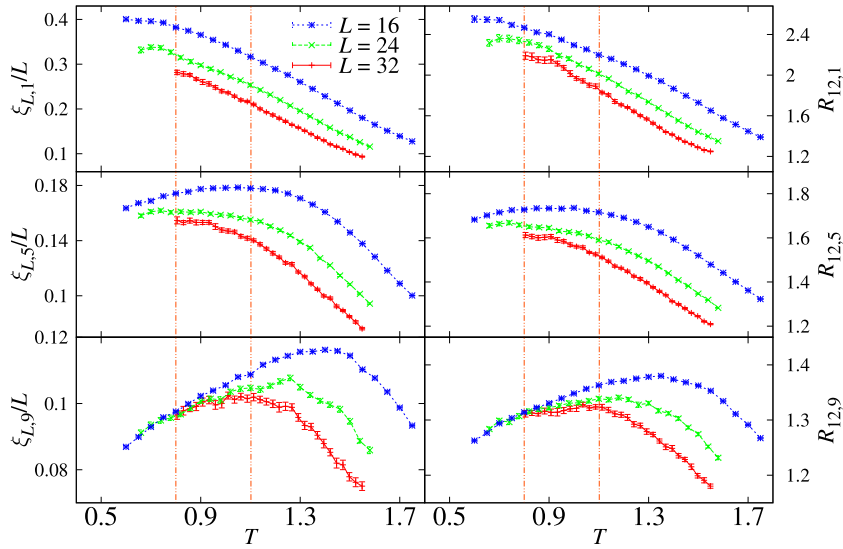


Figure A.1. The same as figure 8, but for $h = 0.1$. This time the effects of the zero-temperature transition are stronger, so we removed from the plot sizes $L = 6, 8, 12$. In appendix D we show that the quantile description is not suitable for smaller lattices due to crossover effects from the zero-field behaviour.

Acknowledgments

We thank M A Moore and J Yeo for pointing out to us the potential usefulness of the Fisher–Sompolinsky scaling.

The Janus project has been partially supported by the EU (FEDER funds, No. UNZA05-33-003, MEC-DGA, Spain), by the European Research Council under the European Union’s Seventh Framework Programme (FP7/2007–2013, ERC grant agreement No. 247328), by MINECO (Spain) (contracts FIS2012-35719-C02, FIS2010-16587, TEC2010-19207), by the SUMA project of INFN (Italy), by the Junta de Extremadura (GR10158) and by the European Union (PIRSSES-GA-2011-295302). FR-T was supported by the Italian Research Ministry through the FIRB project No. RBFR086NN1, MB-J was supported by the FPU programme (Ministerio de Educacion, Spain), RAB and JM-G were supported by the FPI programme (Diputacion de Aragon, Spain) and SP-G was supported by the ARAID foundation; finally JMG-N was supported by the FPI programme (Ministerio de Economia, Spain).

Appendix A. Quantiles for different fields

A.1. Quantiles for $h = 0.1$

The careful reader might have noticed that the upper bound $T^{\text{up}}(h)$ for the possible phase transition given in [34] is higher when the field is lower, $T^{\text{up}}(0.1) = 0.8 > T^{\text{up}}(0.2)$. It is

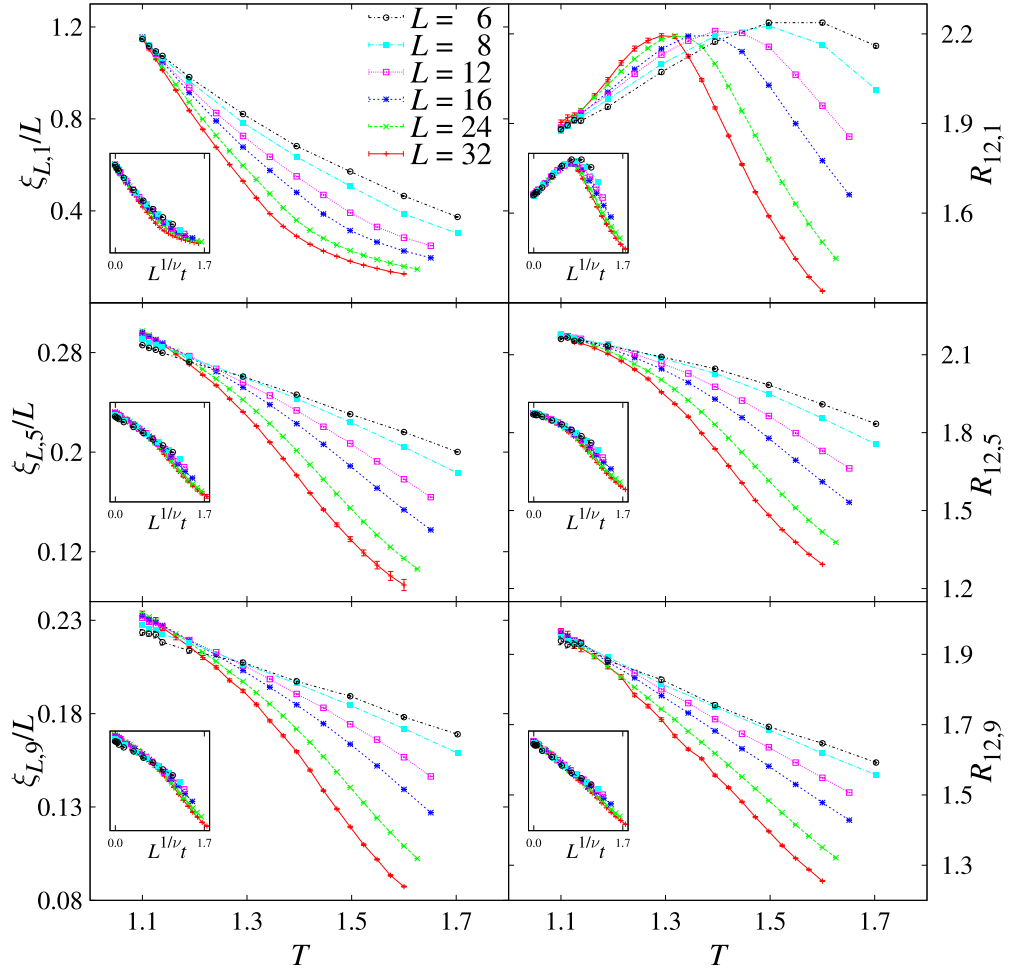


Figure A.2. The same as figure 8, but for $h = 0$. The data come from [51]. We used 256 000 samples for each lattice size. The insets show the same data for the larger sets, but as a function of the scaling variable $L^{1/\nu}t$, where t is the reduced temperature, $t = (T - T_c)/T_c$.

then justified to ask oneself what the quantile plots look like for $h = 0.1$. We show them in figure A.1. Since the field is lower, the effects on the double peak in the first quantile appendix D extend to larger lattices than for $h = 0.2$. Thus, we show only the non-biased sizes, i.e., $L > 12$.

Although the ninth quantile shows signs of scale invariance at $T = T^{\text{up}}(0.1)$, the behaviour of the fifth quantile suggests a scale invariance around $T = 0.5$. We believe that the fifth quantile is a better indicator, since the position of the fifth quantile \tilde{q}_5 has less finite-size effects (it has practically none, figure 6, inset) than \tilde{q}_9 .

It is interesting to focus on the height of the crossings of each quantile, and compare them with $h = 0.2$ (recall figure 8). This is expected to be a universal quantity, and in the hypothesis of a phase transition it should be the same for both fields. Although it is not possible to assign error bars to these values, it is possible to see that for both $h = 0.1$ and $h = 0.2$ the heights are similar ($\xi_{L,5}/L \approx 0.15$, $\xi_{L,9}/L \approx 0.09$, $R_{12,5} \approx 1.6$, $R_{12,9} \approx 1.3$).

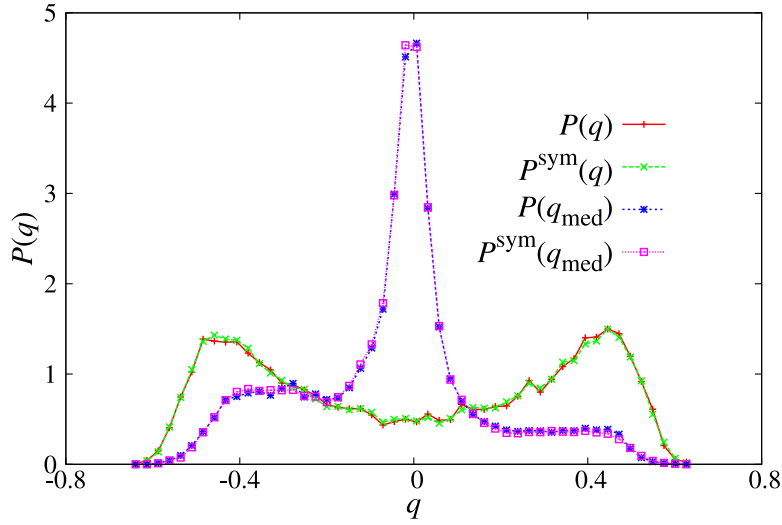


Figure A.3. Probability distribution functions for $h = 0$, $L = 24$, $T = 1.1$. The data come from 512 samples where we took all 16^4 combinations of overlaps per sample. We show $P(q)$, which in null field is symmetric, and $P(q_{\text{med}})$, which is not. We also plot the symmetrized histograms $P^{(\text{sym})}(q)$ and $P^{(\text{sym})}(q_{\text{med}})$.

A.2. Quantiles for $h = 0$

We take advantage of our $h = 0$ data from [51] to validate the quantile description by showing its behaviour in the zero-field case. Two replicas would be sufficient to construct connected correlators in $h = 0$, and use of the four-replica definitions proposed in section 4 only adds noise to the results. However, we opted for the latter option because the objective of the current section is the validation of the full procedure proposed herein.

In the absence of a magnetic field we expect the curves $\xi/L(T)$ and R_{12} to cross no matter which quantile, since the behaviour of the system is not dominated by extreme events and crossover fluctuations. Also, in this case the data in our hands arrive down to the critical point, so the crossings ought to be visible.

In fact, one can see from figure A.2 that all the quantiles show visible signs of a crossing at T_c in the cases of both ξ_L/L and of R_{12} . Furthermore, if we plot the same data as a function of the scaling variable $L^{1/\nu}(T - T_c)/T_c$ the data collapses well for all the quantiles (figure A.2, insets).

Some readers may be surprised that quantiles 1 and 9 show different behaviour, as they are $P(q)$ symmetrical (figure A.3). The reason is that, although $P(q)$ is symmetrical, $P(q_{\text{med}})$ is not. In fact, given six overlaps $q^{ab}, q^{ac}, q^{ad}, q^{bc}, q^{bd}, q^{cd}$ coming from four configurations $\{\sigma^{(a)}\}, \{\sigma^{(b)}\}, \{\sigma^{(c)}\}, \{\sigma^{(d)}\}$, each enjoying a Z_2 symmetry, the distribution of their median advantages negative values¹⁷. We show this in figure A.3, where we give

¹⁷ Let us give a simple example. Take four Z_2 -symmetric single-spin systems that can assume different values $s_1 = \pm 1, s_2 = \pm 2, s_3 = \pm 3, s_4 = \pm 4$. We can construct six overlaps $q_{ij}(s_1, s_2, s_3, s_4)$. If we explicitly impose the Z_2 symmetry, taking all the combinations of our random variables, the histogram of q will be symmetric with zero mean. However, if we take the histogram of the median overlap, it will be asymmetric with mean $\langle q_{\text{med}} \rangle = -3$. This can easily be checked by computing all the possible combinations of the signs of the s_i and computing the median in each case: $q_{\text{med}}(+1, +2, +3, +4) = 5$, $q_{\text{med}}(+1, +2, +3, -4) = -1$, $q_{\text{med}}(+1, +2, -3, -4) = -3.5$, and so on.

both the $P(q)$ and the $P(q_{\text{med}})$ for $h = 0$, $L = 32$, $T = 1.1$. The first is symmetrical and the second is not. To convince the reader that the starting configurations do enjoy Z_2 symmetry, we also construct the symmetrized functions $P^{(\text{sym})}(q)$ and $P^{(\text{sym})}(q_{\text{med}})$. These two functions are obtained by explicitly imposing the Z_2 symmetry: for each measurement we construct the 2^4 overlaps with both $\{\sigma_i\}$ and $\{-\sigma_i\}$. It is visible from figure A.3 that $P^{(\text{sym})}(q_{\text{med}})$ is asymmetric even though we imposed by hand the Z_2 symmetry on the configurations.

Appendix B. Four-replica correlators

In the presence of a magnetic field it is not possible to construct connected correlation functions with the use of only two replicas because in the paramagnetic phase $\overline{\langle q \rangle} = q_{\text{EA}} > 0$.

With four replicas we can construct three different correlators at distance \mathbf{r} ,

$$\begin{aligned} G_1(\mathbf{r}) &= \frac{1}{V} \sum_{\mathbf{x}} \overline{\langle \sigma_{\mathbf{x}} \sigma_{\mathbf{x}+\mathbf{r}} \rangle^2} \\ &= \frac{1}{V} \sum_{\mathbf{x}} \overline{\langle \sigma_{\mathbf{x}}^{(a)} \sigma_{\mathbf{x}+\mathbf{r}}^{(a)} \sigma_{\mathbf{x}}^{(b)} \sigma_{\mathbf{x}+\mathbf{r}}^{(b)} \rangle}, \end{aligned} \quad (\text{B.1})$$

$$\begin{aligned} G_2(\mathbf{r}) &= \frac{1}{V} \sum_{\mathbf{x}} \overline{\langle \sigma_{\mathbf{x}} \sigma_{\mathbf{x}+\mathbf{r}} \rangle \langle \sigma_{\mathbf{x}} \rangle \langle \sigma_{\mathbf{x}+\mathbf{r}} \rangle} \\ &= \frac{1}{V} \sum_{\mathbf{x}} \overline{\langle \sigma_{\mathbf{x}}^{(a)} \sigma_{\mathbf{x}+\mathbf{r}}^{(a)} \sigma_{\mathbf{x}}^{(b)} \sigma_{\mathbf{x}+\mathbf{r}}^{(c)} \rangle}, \end{aligned} \quad (\text{B.2})$$

$$\begin{aligned} G_3(\mathbf{r}) &= \frac{1}{V} \sum_{\mathbf{x}} \overline{\langle \sigma_{\mathbf{x}} \rangle^2 \langle \sigma_{\mathbf{x}+\mathbf{r}} \rangle^2} \\ &= \frac{1}{V} \sum_{\mathbf{x}} \overline{\langle \sigma_{\mathbf{x}}^{(a)} \sigma_{\mathbf{x}+\mathbf{r}}^{(b)} \sigma_{\mathbf{x}}^{(c)} \sigma_{\mathbf{x}+\mathbf{r}}^{(d)} \rangle}. \end{aligned} \quad (\text{B.3})$$

None of those go to zero for large \mathbf{r} , but, in the paramagnetic phase, for large \mathbf{r} they all tend to the same value, q_{EA} . Therefore, to create connected correlators, we can make two linearly independent combinations of them, and obtain the basic connected propagators of the replicated field theory [71]¹⁸

$$G_{\text{R}} = G_1 - 2G_2 + G_3, \quad G_{\text{L}} = G_1 - 4G_2 + 3G_3. \quad (\text{B.4})$$

It is easy to check that these relations imply

$$\begin{aligned} G_{\text{R}}(\mathbf{r}) &= \overline{[\langle \sigma_{\mathbf{x}} \sigma_{\mathbf{x}+\mathbf{r}} \rangle - \langle \sigma_{\mathbf{x}} \rangle \langle \sigma_{\mathbf{x}+\mathbf{r}} \rangle]^2}, \\ G_{\text{L}}(\mathbf{r}) &= 2G_{\text{R}}(\mathbf{r}) - \Gamma_2(\mathbf{r}), \quad \Gamma_2(\mathbf{r}) = \overline{[\langle \sigma_{\mathbf{x}} \sigma_{\mathbf{x}+\mathbf{r}} \rangle^2 - \langle \sigma_{\mathbf{x}} \rangle^2 \langle \sigma_{\mathbf{x}+\mathbf{r}} \rangle^2]}. \end{aligned} \quad (\text{B.5})$$

The definitions in (B.4), valid at equilibrium, were used in [34] in an out-of-equilibrium context, for lattices of size $L = 80$. In that work it had been noticed that the replicon is the only correlator that carries a significant signal.

¹⁸ In the effective field theory the longitudinal (G_{L}) and anomalous (G_{A}) propagators are degenerated.

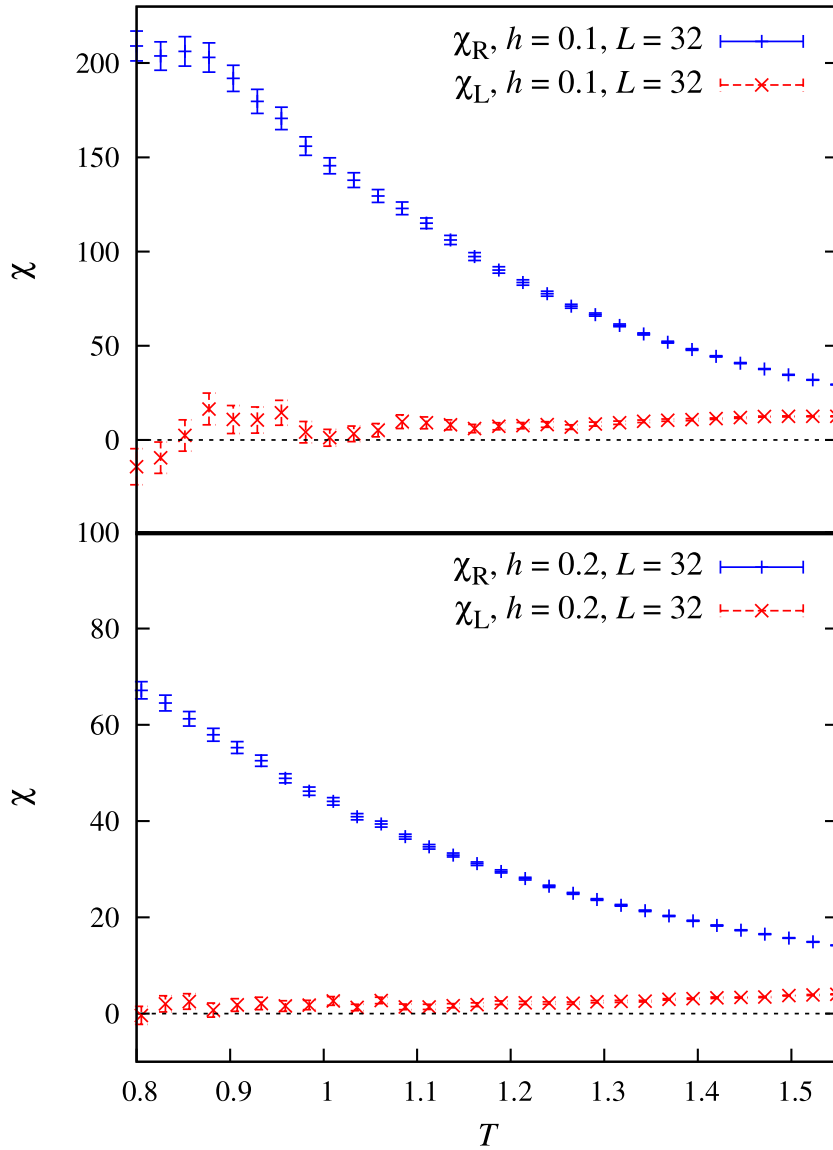


Figure B.1. Replicon and longitudinal susceptibility as a function of T in our equilibrium simulations, for the fields $h = 0.1, 0.2$ in our largest lattice sizes ($L = 32$). Just as in [34] the signal carried by the longitudinal propagator is much smaller than that of the replicon.

Also, in the present work we measured both signals, and we can confirm that the same phenomenology is observed in completely thermalized systems. In figure B.1 we plot both the replicon susceptibility χ_R and the longitudinal susceptibility χ_L , at $h = 0.1, 0.2$. The figure is qualitatively very similar to figure 13 of [34], where it is shown that χ_R carries a significant signal, while χ_L is very close to zero.

B.1. The effective anomalous dimension in the spin-glass phase

We can use the fact that G_R is dominant with respect to G_L to predict the value of the effective anomalous exponent η_{eff} defined in section 9 in the deep spin-glass phase.

In fact, in a replica symmetry breaking (RSB) situation the overlap q has a finite support, so the variance of the overlap $\sigma_q^2 = E(q^2) - E(q)^2$ is of order one,

$$\text{RSB} \Rightarrow \sigma_q^2 \sim 1. \quad (\text{B.6})$$

Now, on general grounds (see for instance [72]) we can expect

$$[E(q^2) - E(q)^2] \sim \overline{\langle q^2 \rangle} - \langle q \rangle^2, \quad (\text{B.7})$$

and remark that the r.h.s. is $\hat{\Gamma}_2(\mathbf{0})/V$, the zero-moment Fourier transform of Γ_2 (defined in (B.5)). We have then that in RSB conditions

$$\Gamma_2(\mathbf{0}) \sim V \sigma_q^2 \stackrel{\text{RSB}}{\sim} V. \quad (\text{B.8})$$

Γ_2 can be related to the replicon and longitudinal susceptibilities through (B.5), which implies that $\Gamma_2(\mathbf{0}) = \chi_R + \frac{1}{2}\chi_L$. Now, at the beginning of this section we found empirically that the longitudinal susceptibility is subdominant with respect to the replicon channel (figure B.1), so in the large-volume limit, in the presence of RSB, the replicon susceptibility scales like the volume,

$$\text{RSB} \Rightarrow \chi_R \sim V. \quad (\text{B.9})$$

Let us recall (29) and impose the just-found implication. We have then

$$2^D \stackrel{\text{RSB}}{\equiv} \frac{\chi_{R,2L}}{\chi_{R,L}} \equiv 2^{2-\eta_{\text{eff}}}; \quad (\text{B.10})$$

therefore, in the spin-glass phase we would have $\eta_{\text{eff}} = -1$.

Appendix C. Technical details on the creation of quantiles

To render our results reproducible, we give some details on how we proceeded in the labelling of the observables with the conditioning variate, and in the definition of the quantiles.

C.1. Creating the $P(\hat{q})$

As already explained in section 3, the analysis we conduct uses instantaneous realizations of the observables, instead of the average over the equilibrium regime. This is because proper computation of $P(\hat{q})$ requires as many instances of the overlap as possible.

Operatively, we divide the second half of the simulation time-series into 16 blocks, and for the four replicas we save the final configuration of each block. This gives us 16^4 configurations over which we can potentially compute overlaps for a single sample. We pick four random numbers between 1 and 16 N_t times to create an instant measure. In this way we increase our statistics by a factor N_t , obtaining $\mathcal{N}_m = N_{\text{samples}}(L, T, h) \times N_t$ measures for each triplet (L, T, h) . We used $N_t = 1000$.

With the four replicas it is possible to compute six different overlaps q_i ($i = 1, \dots, 6$), and one instance of most observables, for example the replicon susceptibility χ_R . Our ansatz is that χ_R and the overlaps have some type of correlation, so we label χ_R with some function of the overlaps $\hat{q}(q_1, \dots, q_6)$, that we call the conditioning variate.

The random variable \hat{q} will have a probability distribution function $P(\hat{q})$ that we want to calculate numerically, in order to be able to work on the quantiles. Since our objective is not to individuate the quantiles exactly, but to compute observables related to a particular quantile, we coarse grain the range of definition of the $P(\hat{q})$. This is carried out by making a binning of the $P(\hat{q})$. In this way, each conditioned expectation value of a generic observable, $E(\mathcal{O}|\hat{q})$, can be calculated over a reasonable amount of measurements, and we have exactly one conditioned expectation value for each bin of the $P(\hat{q})$. Integrals such as those in (18) and (19) are computed as sums over the histogram bins. Furthermore, the described histogramming procedure has the advantage that errors can be calculated in a very natural way with the jackknife method.

In order to have, as L increases, a growing number of both bins and points per bin, we choose bins of width $\Delta\hat{q} = 1/\sqrt{aV}$. We add the restriction of having at least 150 bins, in order to be able to define the quantiles properly (we want to avoid the eventuality of two quantiles between the same two bins). We verified that there is no appreciable difference in the results between $a = 1, 2, 4$. Larger a implies too large an error, because the bins are too small, while with smaller a there are too few bins. The results we show throughout this article have $a = 2$.

To compute the conditional expectation values defined in section 6 we use the following estimators:

$$E(\mathcal{O}|\hat{q} = c) \approx \frac{(1/\mathcal{N}_m) \sum_i^{\mathcal{N}_m} \mathcal{O}_i \mathcal{X}_c(\hat{q}_i)}{(1/\mathcal{N}_m) \sum_i^{\mathcal{N}_m} \mathcal{X}_c(\hat{q}_i)}, \quad (\text{C.1})$$

$$P(\hat{q}) \approx \frac{1}{\mathcal{N}_m} \sum_i^{\mathcal{N}_m} \mathcal{X}_{c=\hat{q}}(\hat{q}_i), \quad (\text{C.2})$$

where by the symbol ‘ \approx ’ we stress that the quantity is an estimator that converges to the exact value only in the limit of an infinite number of measurements.

C.2. Defining the quantiles

As stated in section 7, the quantiles are the points that separate definite areas under $P(\hat{q})$. Therefore, the i th quantile \tilde{q}_i is defined by means of the cumulative distribution $X(\hat{q})$ of $P(\hat{q})$, via the implicit relation

$$X(\tilde{q}_i) = \int_{-1}^{\tilde{q}_i} d\hat{q} P(\hat{q}) = \frac{i}{10}. \quad (\text{C.3})$$

Since this is a continuous relation, and our binning is discrete, it is most probable that the quantile will fall between two neighbouring bins. To evaluate the observables right at the position of the quantile, we make linear interpolations between the two bins.

Let us denote by i_{bin}^- (i_{bin}^+) the bin just under (over) quantile i . Observable \mathcal{O}_i at quantile i will be a linear combination of the values it assumes at i_{bin}^- and i_{bin}^+ ,

$$\mathcal{O}_i = p \mathcal{O}_{i_{\text{bin}}^-} + (1 - p) \mathcal{O}_{i_{\text{bin}}^+}, \quad (\text{C.4})$$

where the interpretation of the indices is straightforward, and $0 \leq p \leq 1$ is the interpolation weight

$$p = \frac{X(\tilde{q}_i) - X(\hat{q}_{\text{bin}}^+)}{X(\hat{q}_{\text{bin}}^-) - X(\hat{q}_{\text{bin}}^+)}. \quad (\text{C.5})$$

Appendix D. A caveat for the quantile description

In the absence of an applied field, the overlap probability distribution function $P(q)$ is symmetric, with a single peak centred in $q = 0$. In the presence of a field, instead, we expect the $P(q)$ to be strictly positive, at least in the thermodynamic limit. Similarly, we expect that the probability distribution function $P(q_{\text{med}})$ will have only one peak at positive q_{med} when a field is applied, and a peak in $q = 0$ if $h = 0$.

If the system sizes are too small, it may occur that the $h = 0$ behaviour biases the $P(q_{\text{med}})$. This is what happens, for example, when $L = 6$, $h = 0.2$ and the temperature is sufficiently low: a second peak around $q_{\text{med}} \simeq 0$ develops upon lowering T (figure D.1, top). This second peak disappears when we increase the lattice size (figure D.1, centre), and the $P(q_{\text{med}})$ assumes only positive values when L is large enough (figure D.1, bottom). The lower the field is, the easier it is to find multiple peaks, and the greater the system has to be to be able to neglect the $h = 0$ behaviour. For $h = 0.05$, even lattices with $L = 12$ show a double peak.

A second peak in $P(q_{\text{med}})$ is a clear signal that we are observing an echo of $h = 0$. When we make the quantile classification, and have a quantile on a peak, we are seeing *only* non-asymptotic data. Thus, quantile 1 for the smallest lattices gives us no relevant information.

If we plot any observable \mathcal{O} related to quantile 1 versus the temperature, the information will be biased for low temperatures, and the bias will gradually disappear as we increase T . The result is that the curve $\mathcal{O}(T)$ will have a strange shape and will be of no use (see, e.g., the $h = 0.05$ data in figure E.1). This is why we did not include the $L = 6$ points in figure 8.

Appendix E. Finding a privileged q

Since all our simulations are in the paramagnetic phase, the thermodynamic limit of the $P(q)$ is a delta function, so all the quantiles should tend to the common $q = q_{\text{EA}}$ in the $L \rightarrow \infty$ limit. We tried to perform these extrapolations at fixed (reasonably low) temperature, to see whether we could look at the problem from such a privileged position. In figure E.1 we see this type of extrapolation for $h = 0.4$ and $h = 0.05$, at temperatures $T = 0.81$ and 1.109 . The first is the lowest temperature we simulated in all our lattices, while the second is the zero-field critical temperature [51]. Since we are in the paramagnetic phase and we are plotting \tilde{q}_i versus the inverse lattice size, the curves should cross at the intercept. This is indeed what appears to happen, but although in the case of $h = 0.4$ the extrapolations were clean, for all the other simulated fields the finite-size effects were too strong and non-linear to make solid extrapolations. We remark, however, that once $L > 8$ the fifth quantile is the one with the least finite-size effects.

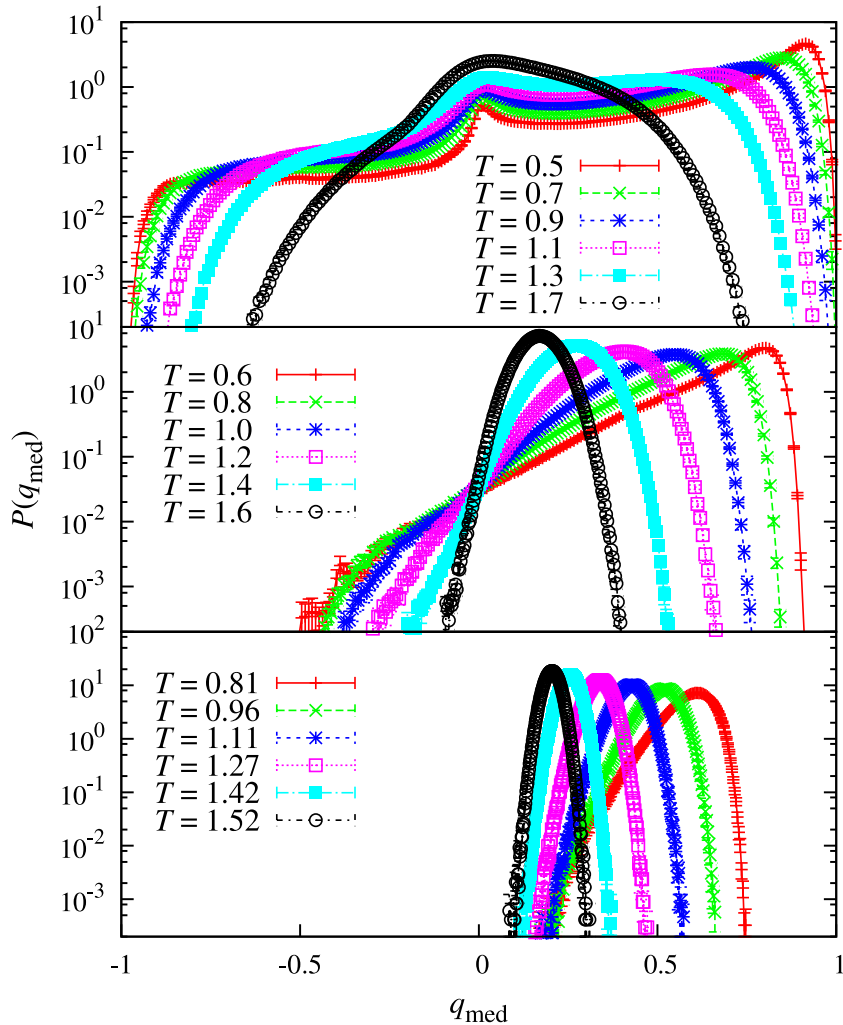


Figure D.1. The median overlap probability distribution function $P(q_{\text{med}})$ with $h = 0.2$ for different temperatures (the ones from $L = 32$ are an approximation to the second decimal digit). The top figure shows the case of $L = 6$, where the lowest temperature curves display a second peak around $q_{\text{med}} \simeq 0$, which disappears when T increases. For $L = 16$, the $P(q_{\text{med}})$ are single-peaked, but assume also negative values. In the bottom curve we have $L = 32$, where the $P(q_{\text{med}})$ are single-peaked and defined only on positive q_{med} , since we are closest to the asymptotic behaviour.

Appendix F. Quantiles with two-replica correlators

To have well behaving (connected) correlators in the presence of a magnetic field we needed to use four replicas for each instance of them. As explained in sections 6 and 7, since the overlap is a two-replica observable, we had to choose a function of the six overlaps in order to have a one-to-one correspondence between the conditioning variates and the correlators. The functions we tried were the minimum, the maximum, the median and the average of the six overlaps.

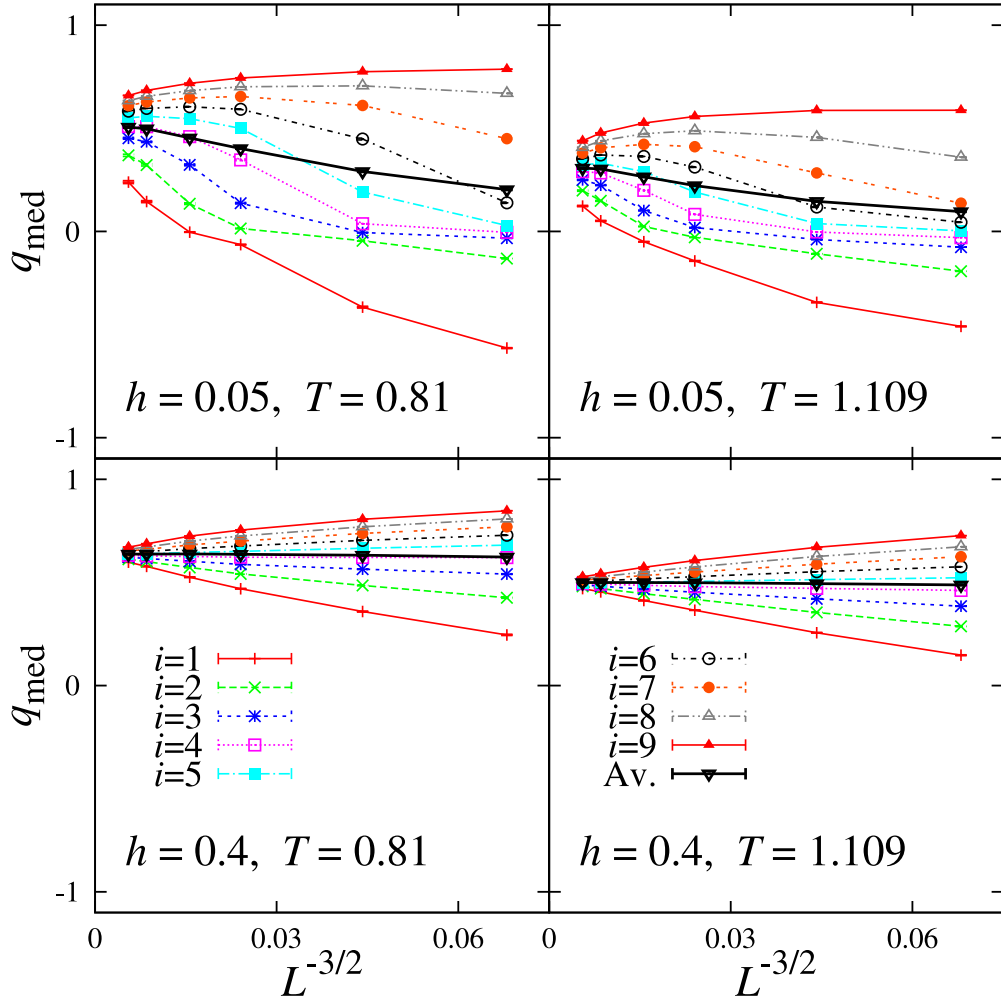


Figure E.1. Extrapolations to infinite size of the quantile overlap \tilde{q}_i , for $T = 0.81$ (left) and $T = 1.109$ (right), and fields $h = 0.05$ (top) and $h = 0.4$ (bottom). We show quantiles $i = 1, \dots, 9$ (thin lines), and the average behaviour (bold line). The $h = 0.4$ extrapolations to infinite volume were clean ($\chi^2/\text{DOF} < 1$), while for $h = 0.05$ (and all the other fields we simulated) we encountered too strong and non-linear finite-size effects to get reasonable extrapolations. We chose $1/L^{D/2}$ as the scaling variable because in conditions of validity of the central limit theorem, the fluctuations should be of order $1/\sqrt{V}$.

Now, it is legitimate to ask oneself whether the fluctuations we observed would also be visible if we had q as the conditioning variate. Although this is not possible with the replicon correlation function G_R , we can renounce the connected correlation function, and study the fluctuations of the two-replica point-to-plane correlator

$$G_2^{\text{nc}}(r) = \sum_{y,z} E(q_{(0,0,0)} q_{(r,y,z)}), \quad (\text{F.1})$$

which allows us to have q as a conditioning variate. $G_2^{\text{nc}}(r)$ is the total correlation between the origin, $(0, 0, 0)$, and the plane, $x = r$. Of course, one could equivalently consider the

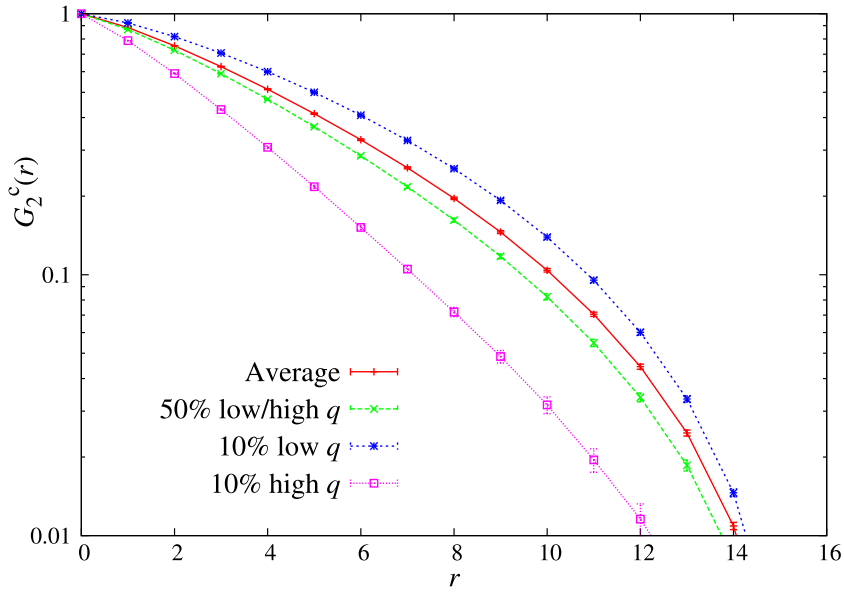


Figure F.1. The same as figure 3, but for the two-replica connected correlation function $G_2^c(r)$ (F.2). We show $L = 32$ data from $h = 0.2$, $T = 0.805128$. Note that $G_2^c(r)$ is bound to be 1 at $r = 0$ and 0 at $r = L/2$, so the fluctuations between different quantiles are even stronger than they may appear.

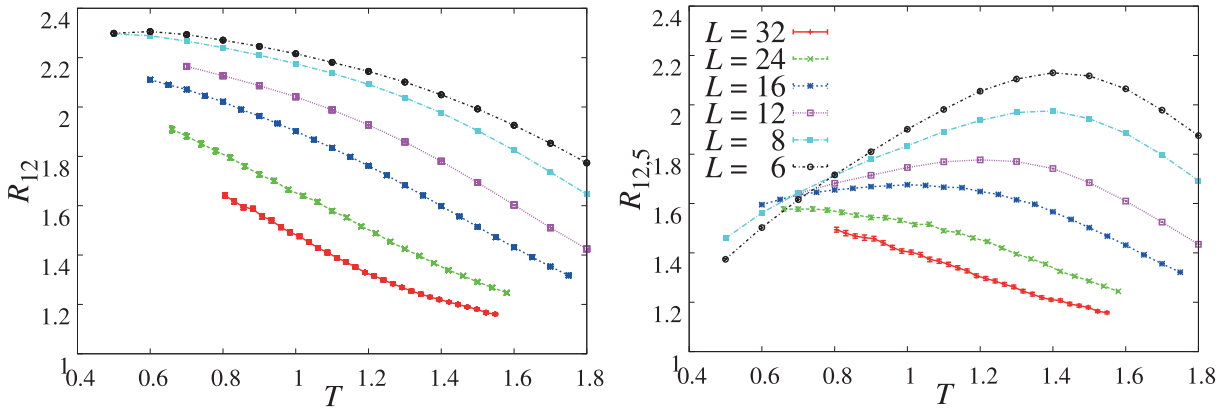


Figure F.2. The R_{12} cumulant computed from the two-replica correlation function (F.1) rather than from four replicas. The field is $h = 0.2$. On the left side we show the average behaviour, and on the right the fifth quantile, with the plain overlap q (3) as the conditioning variate.

planes $y = r$ or $z = r$. One can freely displace the origin as well. We average over all these $3V$ choices.

At this point, it is possible to compare with previous work that studied fluctuations with two-replica correlators [47]. Furthermore, we can construct the pseudoconnected

correlation function

$$G_2^c(r) = \frac{G_2^{\text{nc}}(r) - G_2^{\text{nc}}(L/2)}{G_2^{\text{nc}}(0) - G_2^{\text{nc}}(L/2)}, \quad (\text{F.2})$$

which is forcedly one for $r = 0$, and goes to zero for $r = L/2$. In figure F.1 we show that the same dramatic fluctuations encountered with G_R (figure 3) are also present here.

The overall results, figure F.2, are consistent with the picture we draw in the main part of the paper. On the one hand, the standard data average hides all signs of a phase transition. On the other hand, the fifth quantile displays signs of scale invariance.

Appendix G. High-temperature extrapolation of the critical line

While this paper was being completed, M A Moore and J Yeo pointed out to us that it would be worthwhile to consider the Fisher–Sompolinsky scaling [73] for the correlation-length data from [34]. Since these data were obtained in a very large lattice at comparatively high temperatures, the large fluctuations discussed in this paper should be greatly attenuated. Therefore, the results in [34] are to be regarded as representative of the thermodynamic limit in the paramagnetic phase.

The Fisher–Sompolinsky scaling suggests a possible location of the dAT line in rough agreement with our finite-size scaling analysis at lower temperatures. Let us see how it works.

A standard RG argument (see, e.g., [66]) tells us that, at least for small magnetic fields and close to the zero-field critical temperature, the correlation length should behave as

$$h^{2/y_h} \xi(t, h) = F(t/h^{2y_t/y_h}), \quad (\text{G.1})$$

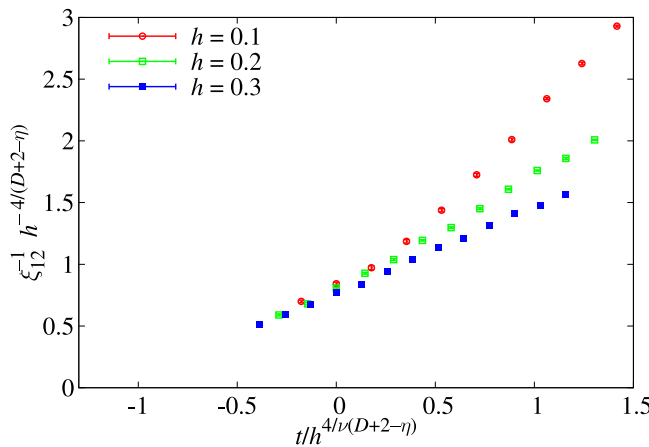


Figure G.1. The ξ_{12} estimate of the correlation length from the thermodynamic-limit data in [34]. We display the data as suggested by the Fisher–Sompolinsky scaling (G.1). We plot $1/\xi$, rather than ξ , in order to identify a possible critical point.

where t is the $h = 0$ reduced temperature, $t = (T - T_c)/T_c$, while the $h = 0$ critical exponents are

$$y_h = \frac{D + 2 - \eta}{2}, \quad y_t = \frac{1}{\nu}. \quad (\text{G.2})$$

We shall assess (G.1) using the estimates of [51]¹⁹.

In figure G.1 we plot $y = 1/[h^{2/y_h}\xi(t, h)]$ as a function of the scaling variable $x = t/h^{2y_t/y_h}$. At the (would-be) dAT line, y should vanish at a critical x_c . In fact, y should behave as $y \sim (x_c - x)^{\nu_h}$ (i.e., ν_h is the correlation-length exponent in a field). Hence, at least for small h , one would have

$$T_c(h) = T_c(h = 0)[1 + x_c h^{2y_t/y_h}]. \quad (\text{G.3})$$

Now, the scaling in figure G.1 is poor, but it improves upon decreasing x (i.e., lowering the temperature). The estimation of x_c depends strongly on the value that one uses for the exponent ν_h . For instance, the rather improbable value $\nu_h = 1$ suggests $x_c \approx -1.2$. With a rather more plausible $\nu_h = \nu \approx 2.56$ one would guess $x_c \approx -0.6$. This disparate range of x_c would predict $T_c(h = 0.1) \approx 0.4\text{--}0.8$, $T_c(h = 0.2) \approx 0.3\text{--}0.7$, $T_c(h = 0.4) \approx 0.1\text{--}0.6$. Overall, these numbers are not in conflict with the finite-size scaling analysis we presented, but they are not of much help in locating the dAT line.

References

- [1] Mydosh J A, 1993 *Spin Glasses: an Experimental Introduction* (London: Taylor and Francis)
- [2] Edwards S F and Anderson P W, 1975 *J. Phys. F: Met. Phys.* **5** 965
- [3] Edwards S F and Anderson P W, 1976 *J. Phys. F: Met. Phys.* **6** 1927
- [4] Mézard M, Parisi G and Virasoro M, 1987 *Spin-Glass Theory and Beyond* (Singapore: World Scientific)
- [5] de Almeida J R L and Thouless D J, 1978 *J. Phys. A: Math. Gen.* **11** 983
- [6] Marinari E, Parisi G, Ricci-Tersenghi F, Ruiz-Lorenzo J J and Zuliani F, 2000 *J. Stat. Phys.* **98** 973 [arXiv:cond-mat/9906076]
- [7] Parisi G, 1979 *Phys. Rev. Lett.* **43** 1754
- [8] Parisi G, 1980 *J. Phys. A: Math. Gen.* **13** 1101
- [9] Parisi G, 1983 *Phys. Rev. Lett.* **50** 1946
- [10] Parisi G and Temesvári T, 2012 *Nucl. Phys. B* **858** 293 [arXiv:1111.3313]
- [11] McMillan W L, 1984 *J. Phys. C: Solid State Phys.* **17** 3179
- [12] Bray A J and Moore M A, *Scaling theory of the ordered phase of spin glasses*, 1987 *Heidelberg Colloquium on Glassy Dynamics (Lecture Notes in Physics vol 275)* ed J L van Hemmen and I Morgenstern (Berlin: Springer)
- [13] Fisher D S and Huse D A, 1986 *Phys. Rev. Lett.* **56** 1601
- [14] Fisher D S and Huse D A, 1988 *Phys. Rev. B* **38** 386
- [15] Moore M A and Bray A J, 2011 *Phys. Rev. B* **83** 224408 [arXiv:1102.1675]
- [16] Yeo J and Moore M A, 2012 *Phys. Rev. E* **86** 052501 [arXiv:1208.3044]
- [17] Jönsson P E, Takayama H, Katori H A and Ito A, 2005 *Phys. Rev. B* **71** 180412(R) [arXiv:cond-mat/0411291]
- [18] Petit D, Fruchter L and Campbell I A, 1999 *Phys. Rev. Lett.* **83** 5130 [arXiv:cond-mat/9910353]
- [19] Petit D, Fruchter L and Campbell I A, 2002 *Phys. Rev. Lett.* **88** 207206 [arXiv:cond-mat/011112]
- [20] Tabata Y, Matsuda K, Kanada S, Yamazaki T, Waki T, Nakamura H, Sato K and Kindo K, 2010 *J. Phys. Soc. Japan* **79** 123704 [arXiv:1009.6115]
- [21] Bray A J and Moore M A, 1980 *J. Phys. C: Solid State Phys.* **13** 419

¹⁹ The correlation length in [34] is not exactly the same as that computed here (technically, it is the so-called ξ_{12} integral estimator [59]). However, the difference is immaterial as far as scaling properties are concerned.

- [22] Temesvári T and De Dominicis C, 2002 *Phys. Rev. Lett.* **89** 097204 [arXiv:cond-mat/0207512]
- [23] Temesvári T, 2008 *Phys. Rev. B* **78** 220401
- [24] Palassini M and Caracciolo S, 1999 *Phys. Rev. Lett.* **82** 5128 [arXiv:cond-mat/9904246]
- [25] Ballesteros H G, Cruz A, Fernandez L A, Martin-Mayor V, Pech J, Ruiz-Lorenzo J J, Tarancon A, Tellez P, Ullod C L and Ungil C, 2000 *Phys. Rev. B* **62** 14237 [arXiv:cond-mat/0006211]
- [26] Gunnarsson K, Svedlindh P, Nordblad P, Lundgren L, Aruga H and Ito A, 1991 *Phys. Rev. B* **43** 8199
- [27] Young A P and Katzgraber H G, 2004 *Phys. Rev. Lett.* **93** 207203 [arXiv:cond-mat/0407031]
- [28] Jörg T, Katzgraber H G and Krzakala F, 2008 *Phys. Rev. Lett.* **100** 197202 [arXiv:0712.2009]
- [29] Baños R A *et al.*, 2012 *Proc. Nat. Acad. Sci. USA* **109** 6452
- [30] Kotliar G, Anderson P W and Stein D L, 1983 *Phys. Rev. B* **27** 602
- [31] Leuzzi L, Parisi G, Ricci-Tersenghi F and Ruiz-Lorenzo J J, 2008 *Phys. Rev. Lett.* **101** 107203
- [32] Larson D, Katzgraber H G, Moore M A and Young A P, 2013 *Phys. Rev. B* **87** 024414 [arXiv:1211.7297]
- [33] Leuzzi L and Parisi G, 2013 *Phys. Rev. B* **88** 224204 [arXiv:1303.6333]
- [34] Baity-Jesi M *et al.*, 2014 *Phys. Rev. E* **89** 032140 [arXiv:1307.4998]
- [35] Belletti F *et al.* (Janus Collaboration), 2009 *Comput. Sci. Eng.* **11** 48
- [36] Alvarez Baños R *et al.* (Janus Collaboration), 2010 *J. Stat. Mech.* P06026 [arXiv:1003.2569]
- [37] Baños R A *et al.*, 2011 *Phys. Rev. B* **84** 174209 [arXiv:1107.5772]
- [38] Baity-Jesi M *et al.*, 2012 *Eur. Phys. J. Spec. Top.* **210** 33 [arXiv:1204.4134]
- [39] Debenedetti P G, 1997 *Metastable Liquids* (Princeton, NJ: Princeton University Press)
- [40] Debenedetti P G and Stillinger F H, 2001 *Nature* **410** 259
- [41] Cavagna A, 2009 *Phys. Rep.* **476** 51 [arXiv:0903.4264]
- [42] Castellani T and Cavagna A, 2005 *J. Stat. Mech.* P05012
- [43] Kirkpatrick T R and Thirumalai D, 1987 *Phys. Rev. B* **36** 5388
- [44] Kirkpatrick T R, Thirumalai D and Wolynes P G, 1989 *Phys. Rev. A* **40** 1045
- [45] Moore M A and Drossel B, 2002 *Phys. Rev. Lett.* **89** 217202 [arXiv:cond-mat/0201107]
- [46] Fullerton C J and Moore M A, 2013 [arXiv:1304.4420]
- [47] Parisi G and Ricci-Tersenghi F, 2012 *Phil. Mag. B* **92** 341 [arXiv:1108.0759v1]
- [48] Nightingale M P, 1975 *Physica A* **83** 561
- [49] Binder K, 1982 *Phys. Rev. A* **25** 1699
- [50] Ballesteros H G, Fernandez L A, Martin-Mayor V, Muñoz Sudupe A, Parisi G and Ruiz-Lorenzo J J, 1998 *Nucl. Phys. B* **512** 681
- [51] Baity-Jesi M *et al.* (Janus Collaboration), 2013 *Phys. Rev. B* **88** 224416 [arXiv:1310.2910]
- [52] Baity-Jesi M, Fernandez L A, Martin-Mayor V and Sanz J M, 2014 *Phys. Rev. B* **89** 014202 [arXiv:1309.1599]
- [53] Lee L W and Young A P, 2003 *Phys. Rev. Lett.* **90** 227203
- [54] Jörg T, 2006 *Phys. Rev. B* **73** 224431
- [55] Fernandez L A, Martin-Mayor V and Yllanes D, 2011 *Phys. Rev. B* **84** 100408(R)
- [56] Campos I, Cotallo-Aban M, Martin-Mayor V, Perez-Gaviro S and Tarancon A, 2006 *Phys. Rev. Lett.* **97** 217204
- [57] Baños R A, Fernandez L A, Martin-Mayor V and Young A P, 2012 *Phys. Rev. B* **86** 134416 [arXiv:1207.7014]
- [58] Fernandez L A, Martin-Mayor V, Parisi G and Seoane B, 2013 *Eur. Phys. Lett.* **103** 67003 [arXiv:1307.2361]
- [59] Belletti F *et al.* (Janus Collaboration), 2009 *J. Stat. Phys.* **135** 1121 [arXiv:0811.2864]
- [60] Hukushima K and Nemoto K, 1996 *J. Phys. Soc. Japan* **65** 1604 [arXiv:cond-mat/9512035]
- [61] Marinari E, *Optimized Monte Carlo methods*, 1998 *Advances in Computer Simulation* ed J Kerstész and I Kondor (Berlin: Springer)
- [62] Newman M E J and Barkema G T, 1999 *Monte Carlo Methods in Statistical Physics* (Oxford: Clarendon)
- [63] Fernandez L A, Martin-Mayor V, Perez-Gaviro S, Tarancon A and Young A P, 2009 *Phys. Rev. B* **80** 024422
- [64] Yllanes D, *Rugged free-energy landscapes in disordered spin systems*, 2011 *PhD Thesis UCM* [arXiv:1111.0266]
- [65] de Dominicis C and Giardina I, 2006 *Random Fields and Spin Glasses* (Cambridge: Cambridge University Press)
- [66] Amit D J and Martin-Mayor V, 2005 *Field Theory, the Renormalization Group and Critical Phenomena* 3rd edn (Singapore: World Scientific) www.worldscientific.com/worldscibooks/10.1142/5715
- [67] Ballesteros H G, Fernandez L A, Martin-Mayor V and Muñoz Sudupe A, 1996 *Phys. Lett. B* **378** 207 [arXiv:hep-lat/9511003]
- [68] Fernandez L A and Martin-Mayor V, 2009 *Phys. Rev. E* **79** 051109
- [69] Baños R A *et al.* (Janus Collaboration), 2010 *Phys. Rev. Lett.* **105** 177202 [arXiv:1003.2943]

- [70] Hyndman R and Fan Y, 1996 *Am. Stat.* **50** 361
- [71] de Dominicis C, Kondor I and Temesvári T, *Beyond the Sherrington–Kirkpatrick model*, 1998 *Spin Glasses and Random Fields* ed A P Young (Singapore: World Scientific) [arXiv:[cond-mat/9705215](https://arxiv.org/abs/cond-mat/9705215)]
- [72] Fisher K and Hertz J, 1991 *Spin Glasses* (Cambridge: Cambridge University Press)
- [73] Fisher D S and Sompolinsky H, 1985 *Phys. Rev. Lett.* **54** 1063